

Relative merits and limiting factors for x-ray and electron microscopy of thick, hydrated organic materials (2020 revised version)

Ming Du¹, and Chris Jacobsen^{2,3,4,*}

¹Department of Materials Science and Engineering, Northwestern University, 2145 Sheridan Road, Evanston IL 60208, USA

²Advanced Photon Source, Argonne National Laboratory, 9700 South Cass Avenue, Argonne IL 60439, USA

³Department of Physics & Astronomy, Northwestern University, 2145 Sheridan Road, Evanston IL 60208, USA

⁴Chemistry of Life Processes Institute, Northwestern University, 2170 Campus Drive, Evanston IL 60208, USA

*Corresponding author; Email: cjacobsen@anl.gov

Abstract

Electron and x-ray microscopes allow one to image the entire, unlabeled structure of hydrated materials at a resolution well beyond what visible light microscopes can achieve. However, both approaches involve ionizing radiation, so that radiation damage must be considered as one of the limits to imaging. Drawing upon earlier work, we describe here a unified approach to estimating the image contrast (and thus the required exposure and corresponding radiation dose) in both x-ray and electron microscopy. This approach accounts for factors such as plural and inelastic scattering, and (in electron microscopy) the use of energy filters to obtain so-called “zero loss” images. As expected, it shows that electron microscopy offers lower dose for specimens thinner than about 1 μm (such as for studies of macromolecules, viruses, bacteria and archaeobacteria, and thin sectioned material), while x-ray microscopy offers superior characteristics for imaging thicker specimen such as whole eukaryotic cells, thick-sectioned tissues, and organs. The required radiation dose scales strongly as a function of the desired spatial resolution, allowing one to understand the limits of live and frozen hydrated specimen imaging. Finally, we consider the factors limiting x-ray microscopy of thicker materials, suggesting that specimens as thick as a whole mouse brain can be imaged with x-ray microscopes without significant image degradation should appropriate image reconstruction methods be identified. The as-published article [[Ultramicroscopy](#) **184**, 293–309 (2018); doi:10.1016/j.ultramic.2017.10.003] had some minor mistakes that we correct here, with all changes from the as-published article shown in blue.

Key words: x-ray, electron, thick specimen, radiation damage

1 Introduction

Soft materials are often wet materials. This applies to polymer gel absorbants, biofilms in soils, and in particular to biological specimens. While tremendous advances have been made in superresolution light microscopy for the study of added fluorophores or genetically-encoded fluorescent regions in proteins, it is still desirable to image the entirety of a specimen using its intrinsic contrast to provide overall structural context and for this the classical resolution limit of $\delta = 0.61\lambda/\text{NA}$ applies. Given the numerical aperture of wet or oil immersion lenses, this means that it is difficult to see sub-100 nm intrinsic detail in soft materials using visible light microscopes, even when using methods such as structured illumination microscopy [1].

For higher resolution, one must use radiation with a shorter wavelength λ , which is provided in both electron and x-ray microscopes. However, these shorter wavelength probes come at a cost in loss of convenience and, more fundamentally, a cost in terms of radiation damage caused by the use of ionizing radiation. For simple linear effects in molecules, Burton proposed [2] a measure called the G value which is the number of irreversible molecular damage events caused per 100 eV of absorbed energy. While G values for organic molecules span a wide range (such as 0.7 for styrene and 12 for methyl methacrylate at low dose rates [3]),

a geometrical mean of 2.9 implies that a molecular bond is broken for every 35 eV of ionizing radiation deposited. The limitations of radiation damage can be greatly reduced by working with specimens at cryogenic temperatures, as has been learned first in x-ray crystallography [4, 5], and later in electron [6, 7] and then x-ray microscopy [8, 9]. This is done in part by reducing secondary chemical damage effects caused by the radiolysis of water, as these radiolysis products do not diffuse through ice at liquid nitrogen temperatures in the same way as they do in water at room temperature. An additional benefit of cryogenic conditions is that scissioned molecular fragments remain in place, unlike with room temperature specimens in vacuum [10] or in solution. However, because cryogenic imaging conditions reduce but do not eliminate the limitations due to radiation damage, it remains important to understand the relative radiation dose associated with electron and x-ray microscopy for various specimen types.

1.1 Comparisons of electron and x-ray microscopy

The relative merits of electron and x-ray microscopy for transmission imaging have been considered by several researchers who have reached seemingly contradictory conclusions:

- **Molecular imaging can be done at significantly lower radiation dose in electron microscopy than in x-ray microscopy [11, 12].** This conclusion is based on comparing fundamental scattering parameters for electrons as against those for x-rays while seeking to form images using elastically scattered quanta. For 300 keV electrons incident on carbon, the inelastic scattering cross section is only $1.7\times$ larger than that for elastic scattering, and each inelastic scattering event deposits only about 39 eV of energy as will be seen following Eq. 103; this means that only about 66 eV of energy is deposited per elastic scattering event, or 1650 eV if 25 elastically scattered photons are required to obtain a signal to noise ratio of 5. This is about 500 times higher than the ~ 3 eV damage threshold for irreversible bond breaking in organic molecules, making it effectively impossible to obtain atomic resolution images of molecules [11, 13, 12] (unless of course one combines data from low-dose images of many identical molecules [14, 15, 16]). However, ~ 66 eV per molecule per elastically scattered electron is dramatically lower than what happens with 10 keV x-rays, where the photoelectric absorption cross section is about 13 times higher than the elastic scattering cross section for carbon, and moreover photoelectric absorption involves the deposition of the entire energy of the x-ray photon; this means that about 130,000 eV of energy is deposited per elastically scattered x-ray photon. The one exception to this pessimistic view of atomic resolution x-ray imaging might be if the entire x-ray scattering signal can be collected in tens of femtoseconds, during which time inertia might hold the molecule together [17, 18]. While a similar femtosecond imaging approach has been contemplated using electrons [19], Coulomb repulsion amongst charged particles represents a significant challenge [20].
- **X-rays offer great advantages in penetration, so for studies of thicker biological materials it has been argued that soft x-ray microscopy can be carried out at a much lower radiation dose than is the case with electron microscopy [21, 22].** These calculations showed that the greater penetrating power of x-rays was of great advantage for imaging hydrated organic specimens of the size of eukaryotic cells. While they played an important role in motivating the development of x-ray microscopes, these earlier calculations left out several ingredients. In the case of x-ray microscopy, they overlooked the possibility of phase contrast, which greatly reduces contrast and reduces dose at multi-keV x-ray energies [23] (this oversight was rectified in later calculations for x-ray microscopy [24, 25, 26, 8, 27]). These early calculations [21, 22] were done without awareness of the then-recent introduction of defocus phase contrast [28, 29] in electron microscopy. They also predated the introduction of zero-loss filtering, where an imaging energy filter is used to remove inelastically scattered electrons from the final image [30, 31] which otherwise contribute an out-of-focus image “haze.”

In fact, these conclusions are neither contradictory, nor individually incorrect as will be seen in Sec. 7.2. It is our purpose here to use the same calculation methodology for modern approaches to electron and x-ray microscopy to re-evaluate the relative advantages of these methods for different biological specimen types, and also consider the ultimate thickness limits for x-ray microscopy over a wide range of photon energies.

In the case of electron microscopy, several authors have considered the improvements that phase contrast and zero-loss filtering can provide for imaging thicker specimens. In one case, Monte Carlo numerical

Contrast parameter Θ	Equation number
X-rays, thin specimen, absorption contrast	Eq. 22
X-rays, thin specimen, phase contrast, no phase ring absorption	Eq. 36
X-rays, thick specimen, absorption contrast, ignoring inelastic and plural elastic scattering	Eq. 21
X-rays, thick specimen, phase contrast, ignoring inelastic and plural elastic scattering	Eq. 35
X-rays, unified complete expression	Eq. 88
Electrons, phase contrast, without zero-loss energy filtering	Eq. 129
Electrons, phase contrast, with zero-loss energy filtering	Eq. 130

Table 1: Contrast parameters Θ for various imaging modes and degrees of approximation. Once the contrast parameter Θ (defined in Eq. 7) and desired signal to noise ratio SNR are specified, one can calculate the required exposure per pixel \bar{n} using Eq. 8, and the associated radiation dose using Eq. 92 for x-rays or Eq. 131 for electrons.

calculations were used to consider the fraction of electrons that were scattered elastically and inelastically, or that had not scattered at all, leading to estimates of an improved signal-to-noise ratio for zero-loss imaging [32]. Increased insight can be obtained by using not a numerical Monte Carlo model but an analytical approach, since one can then find maxima of the resulting mathematical functions. One such approach added consideration of electrons elastically scattered by large enough angles that they are excluded by the objective lens aperture [33]. Another approach [34] estimated the increased dose requirement in thicker specimens by scaling a single projection image dose up by the number of tilts required to maintain an equivalent 3D resolution in specimens of increasing thickness [35] as quantified by the Crowther criterion [36]. However, for thicker specimens one needs to consider plural elastic scattering within the angle subtended by the objective lens aperture as another undesired background signal, and we are unaware of calculations of image contrast and required dose for electron microscopy that include this effect beyond our own brief report [26]. In addition, while this brief work included phase contrast in x-ray microscopy, it did not consider the role of inelastic or plural elastic x-ray scattering, effects that we include in this present work.

2 Calculation methodology

Our x-ray microscopy calculations are based on estimating image intensities with features present and absent, following the method of certain previous approaches for transmission imaging [13, 21, 24, 25, 26, 8, 37] as well as for x-ray fluorescence imaging [38, 39]. An alternative approach is to consider the scattering strength of small features [17, 40, 41, 42, 43, 44, 45]. The results from these other calculations are broadly similar to the thin specimen results from the method used here. However, those other calculations did not make the comparison with electron microscopy nor did they include effects like plural elastic scattering or inelastic scattering. Estimations of the required exposure and dose have been made for x-ray tomography at higher energies [46], but those calculations predated the realization of the advantages of phase contrast in x-ray tomography.

Our calculations here are for two dimensional images of features with a thickness equal to the intended lateral resolution (that is, we assume that small features have the same size in depth as they do laterally in a 2D image). However, they should apply equally well to 3D imaging on the basis of using dose fractionation, which is the idea that “a three-dimensional reconstruction requires the same integral dose as a conventional two-dimensional micrograph provided that the level of significance and the resolution are identical” [47]. While originally controversial [48], this concept has entered practice and it has withstood the test of simulations [49]. In addition, it is an implicit assumption in the successful method of single-particle imaging [14, 15, 16].

In what follows, we will start with more basic models and consider their limits for the case of thin specimens, after which more complete models will be discussed. A guide to these various expressions is provided in Table 1.

2.1 Image statistics

If all other noise sources are eliminated, the signal-to-noise ratio of an image is dominated by photon statistics [50]. This is properly described by the Poisson distribution, which states that an individual measurement will result in a probability distribution of results $P(n, \bar{n})$ of

$$P(n, \bar{n}) = \frac{\bar{n}^n}{n!} \exp(-\bar{n}) \quad (1)$$

where \bar{n} is the average over many measurements and n is the result of a particular measurement. For values of \bar{n} above about 10, the Poisson distribution is well approximated by a Gaussian distribution of

$$P(n, \bar{n}) = \frac{1}{\sqrt{2\pi\bar{n}}} \exp \left[-\frac{(n - \bar{n})^2}{2\bar{n}} \right] \quad (2)$$

which has a variance σ^2 characterized by

$$\sigma = \sqrt{\bar{n}}. \quad (3)$$

We then follow previous work [13, 21] and consider the signal to be given by the unit-normalized image intensity I_f at the location of a feature f if it is present, versus the intensity I_b of the background material b at the same location if the feature is absent. If we illuminate this image pixel with \bar{n} photons on average, the signal S is then given by

$$S = \bar{n}|I_f - I_b|. \quad (4)$$

The noise is the fluctuation due to photon statistics in both the feature-present and feature-absent cases, since we are looking at the difference between these two cases in Eq. 4. The statistical fluctuations of Eq. 3 in these two measurements are uncorrelated, so the noise N is the root-mean-squared sum of these two results or

$$N = \sqrt{(\sqrt{\bar{n}}I_f)^2 + (\sqrt{\bar{n}}I_b)^2} = \sqrt{\bar{n}}\sqrt{I_f + I_b}. \quad (5)$$

Consequently, the signal-to-noise ratio (SNR) is given by

$$\begin{aligned} SNR &= \sqrt{\bar{n}} \frac{|I_f - I_b|}{\sqrt{I_f + I_b}} \\ &= \sqrt{\bar{n}}\Theta \end{aligned} \quad (6)$$

where we define

$$\Theta = \frac{|I_f - I_b|}{\sqrt{I_f + I_b}} \quad (7)$$

as an image contrast parameter. Therefore we obtain the result that the mean number of quanta \bar{n} with which we must illuminate each pixel in a 2D image (or each voxel in a 3D tomographic reconstruction [47]) is given by [13, 21]

$$\bar{n} = \frac{SNR^2}{\Theta^2}. \quad (8)$$

Human vision studies suggest a signal-to-noise ratio of $SNR = 5$ leads to acceptable image quality (the so-called ‘‘Rose criterion’’ [50]), in which case we arrive at an expression of

$$\bar{n} = \frac{25}{\Theta^2} \quad (9)$$

for the minimum photon exposure per pixel.

2.2 Specimen model

Our specimen model follows the assumption of several previous studies [13, 21]. We consider the feature f material to be in a cube of thickness t_f which is also equal to its transverse dimension (the spatial resolution

in the image). It is contained within a matrix of a background material b with thicknesses $t_{b,o}$ and $t_{b,u}$ over and under the feature, respectively, so that the total specimen thickness t is given by

$$t = t_{b,o} + t_f + t_{b,u} \quad (10)$$

while the total for the underlying and overlying material is

$$t_b = t_{b,o} + t_{b,u} \quad (11)$$

as shown in Figure 1. Therefore t_f might represent the reconstructed voxel size in tomographic imaging, where again we assume that dose fractionation applies [47].

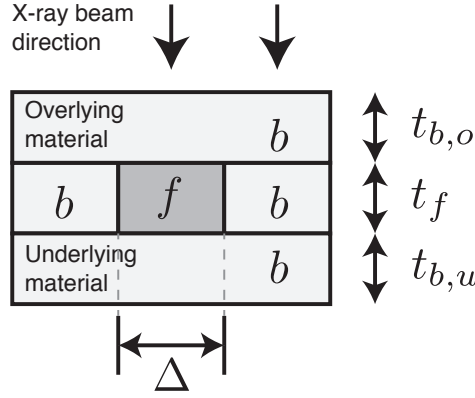


Figure 1: Schematic diagram of the specimen model adopted for contrast parameter calculations. Features of material f are assumed to be cubes of dimension t_f on a side, embedded in an overall matrix thickness of $t = t_{b,o} + t_f + t_{b,u}$ of background material b . For biological imaging, we will assume that the feature f is composed of protein, and the background material b is amorphous ice.

For biological materials we will follow the assumption that the feature f is comprised of the stoichiometric composition of a representative protein formed from the average of all 20 amino acids, leading to a composition of $\text{H}_{48.6}\text{C}_{32.9}\text{N}_{8.9}\text{O}_{8.9}\text{S}_{0.6}$ with a density when dry of 1.35 g/cm^3 [41]. This likely slightly overestimates the contrast of features f , since even densely-packed macromolecules contain appreciable water. We will assume that the bulk of the mass of a biological specimen is comprised of one of two materials: amorphous ice with a density of 0.92 g/cm^3 for frozen hydrated biological specimens [51], or the embedding medium EPON for dehydrated specimens for which we assume a stoichiometric composition of $\text{C}_{18}\text{H}_{21}\text{O}_3\text{Cl}$ and a density of 1.20 g/cm^3 .

3 Image contrast in x-ray microscopy

We first consider the case of image contrast and dose x-ray microscopy. We begin with a simplified model in Sec. 3.1 which follows earlier calculation methods [21, 52]. We then consider the additional factors of inelastic and plural elastic scattering and arrive at a more complete model in Sec. 4.

3.1 X-ray microscopy: simplified model

Materials illuminated by x-ray beams have an index of refraction n that is slightly less than unity [53, 54] which can be written as

$$n = 1 - \delta - i\beta. \quad (12)$$

An alternative expression is

$$n = 1 - \alpha\lambda^2(f_1 + if_2) \quad (13)$$

with

$$\alpha \equiv \frac{r_e}{2\pi} n_a, \quad (14)$$

where r_e is the classical radius of the electron, n_a is the number density of atoms, and $(f_1 + if_2)$ describes the frequency-dependent complex number of oscillator modes per atom in a form for which excellent tabulations exist [55, 56, 57].

The simplest contrast mechanism for x-ray imaging is absorption, for which a transmitted beam has an intensity

$$I = I_0 \exp(-\mu t) \quad (15)$$

according to the Lambert-Beer law. Here μ is a linear absorption coefficient that can be found from

$$\mu = \frac{4\pi}{\lambda} \beta = 4\pi\alpha\lambda f_2. \quad (16)$$

For the specimen model shown in Fig. 1, the image intensity with a feature present is given by

$$\begin{aligned} I_{f,\text{abs}} &= I_0 \exp(-\mu_f t_f) \exp(-\mu_b t_{b,o}) \exp(-\mu_b t_{b,u}) \\ &= I_0 \exp(-\mu_f t_f) \exp(-\mu_b t_b) \end{aligned} \quad (17)$$

while the feature absent (background) case is given by

$$\begin{aligned} I_{b,\text{abs}} &= I_0 \exp(-\mu_b t_{b,o}) \exp(-\mu_b t_f) \exp(-\mu_b t_{b,u}) \\ &= I_0 \exp(-\mu_b t). \end{aligned} \quad (18)$$

In the limits of $\mu_t t_f \ll 1$ and $\mu_b t_f \ll 1$, the above equations can be simplified as

$$I_{f,\text{abs}} \approx I_0 (1 - \mu_f t_f) \exp(-\mu_b t_b) \quad (19)$$

and

$$I_{b,\text{abs}} \approx I_0 (1 - \mu_b t_f) \exp(-\mu_b t_b). \quad (20)$$

Letting $I_0 = 1$ for unit-normalized intensities in accordance with the expression of Eq. 7, we arrive at a contrast parameter Θ_{abs} for x-ray absorption contrast imaging of

$$\begin{aligned} \Theta_{\text{abs}} &= \frac{|I_{f,\text{abs}} - I_{b,\text{abs}}|}{\sqrt{I_{f,\text{abs}} + I_{b,\text{abs}}}} \exp(-\mu_b t_b/2) \\ &= \frac{|\exp(-\mu_f t_f) - \exp(-\mu_b t_f)|}{\sqrt{\exp(-\mu_f t_f) + \exp(-\mu_b t_f)}} \exp(-\mu_b t_b/2) \end{aligned} \quad (21)$$

which for thin specimens becomes

$$\Theta_{\text{abs}} \approx \frac{t_f}{\sqrt{2}} |\mu_f - \mu_b| \exp(-\mu_b t_b/2) \quad (22)$$

$$\approx \frac{2\pi\sqrt{2}}{\lambda} t_f |\beta_f - \beta_b| \exp(-\mu_b t_b/2) \quad (23)$$

as expressed using either the linear absorption coefficients μ for Eq. 22 or the amplitude reduction part β of the complex x-ray refractive index (Eq. 12) for Eq. 23.

While it has long been known that the phase-shifting part δ of the x-ray refractive index is much larger than the amplitude-reducing part β , it was not until 1987 that Schmahl and Rudolph suggested the use of phase contrast in x-ray imaging [23]. They considered the case of using the Zernike method [58, 59, 60] in x-ray microscopes, and arrived at expressions for the image contrast [52] which we will briefly restate here. (There are a number of approaches to obtaining phase contrast x-ray images which produce broadly similar results [61]; the Zernike method has the advantage of allowing for a direct calculation of image intensities as required for the contrast parameter Θ , and that is why we use it here). Zernike phase contrast in x-ray microscopy involves a linear phase coefficient

$$\eta_i = 2\pi \frac{\delta_i}{\lambda} \quad (24)$$

for phase advance per thickness in the materials of the feature ($i \rightarrow f$), the background ($i \rightarrow b$), and the phase ring ($i \rightarrow p$). The original derivation began from formulating the complex amplitudes A of waves exiting from the feature-present (A_f) and -absent (A_b) regions. We slightly modify the equations to adapt them to the specimen model used in this work, which contains an overlaying background layer on the dispersed feature materials, leading to

$$A_f = A_0 \exp[-(\mu_b/2)t_b] \exp[i\eta_b t_b] \exp[-(\mu_f/2)t_f] \exp[i\eta_f t_f] \quad (25)$$

$$A_b = A_0 \exp[-(\mu_b/2)t_b] \exp[i\eta_b t_b] \exp[-(\mu_b/2)t_f] \exp[i\eta_b t_f]. \quad (26)$$

The amplitude attenuation and phase shift imposed upon the reference beam A_b by transmission T through the phase ring is

$$T_p = \exp[-(\mu_p/2)t_p] \exp(i\eta_p t_p). \quad (27)$$

As a result, the amplitude of the reference beam on the image plane is given by

$$A'_b = A_b T_p \quad (28)$$

while the wave A_d diffracted due to the presence of feature rather than background material in the pixel t_f is

$$A_d = A_f - A_b. \quad (29)$$

Because of its scattering throughout the lens aperure, the diffracted wave A_d is nearly unaffected by the modulation T_p of the small phase ring. As a result, the amplitude of the wave that transmits through feature-present regions of the specimen takes the following form at the image plane:

$$A'_f = A'_b + A_d = A'_b + (A_f - A_b). \quad (30)$$

Therefore the detected image intensities for the feature-present and -absent cases are given by

$$\begin{aligned} I_{f,\text{zpc}} &= A_f A_f^* \\ &= e^{-\mu_b(t_b - t_f)} \left[(1 + e^{\mu_p t_p}) e^{-\mu_b t_f} + e^{-\mu_f t_f} + \right. \\ &\quad \left. 2e^{-\mu_f t_f/2 - \mu_b t_f/2} \cos(\eta_f t_f - \eta_b t_f - \eta_p t_p) - \right. \\ &\quad \left. 2e^{-\mu_f t_f/2 - \mu_b t_f/2} \cos(\eta_f t_f - \eta_b t_f) - 2e^{-\mu_b t_f - \mu_p t_p/2} \cos(\eta_p t_p) \right] \end{aligned} \quad (31)$$

$$\begin{aligned} I_{b,\text{zpc}} &= A_b A_b^* \\ &= e^{-\mu_b(t_b - t_f)} e^{-\mu_b t_f - \mu_p t_p}. \end{aligned} \quad (32)$$

If the specimen is a weak phase object, and the phase ring produces a phase shift of exactly $\pi/2$ with no absorption, these expressions reduce to

$$I_{f,\text{zpc}} \approx I_0 [1 + 2(\eta_f - \eta_b)t_f] \exp(-\mu_b t_b) \quad (33)$$

$$I_{b,\text{zpc}} \approx I_0 \exp(-\mu_b t_b). \quad (34)$$

We then have a contrast parameter for Zernike phase contrast imaging of

$$\Theta_{\text{zpc}} = \frac{|I_{f,\text{zpc}} - I_{b,\text{zpc}}|}{\sqrt{I_{f,\text{zpc}} + I_{b,\text{zpc}}}} \quad (35)$$

involving the expressions of Eqs. 31 and 32. In the weak phase contrast limits of $t_f \eta_f \ll 1$ and $t_f \eta_b \ll 1$, this can be simplified by using Eqs. 33 and 34 to arrive at

$$\Theta_{\text{zpc}} \approx \sqrt{2} t_f |\eta_f - \eta_b| \exp(-\mu_b t_b/2) \quad (36)$$

$$\approx \frac{2\pi\sqrt{2}}{\lambda} t_f |\delta_f - \delta_b| \exp(-\mu_b t_b/2) \quad (37)$$

where Eq. 37 emphasizes the symmetry with Eq. 23.

We have seen that the contrast parameters of the two imaging schemes mentioned depend on the x-ray refractive indices $1 - \delta_f - i\beta_f$ for the feature material, and $n = 1 - \delta_b - i\beta_b$ for the background material. With these expressions in the thin specimen limit (Eqs. 23 and 37), one can use Eq. 8 to formulate simplified expressions for the number of photons \bar{n} required for imaging at the Rose criterion of $SNR = 5$ of

$$\bar{n}_{\text{abs}} = \frac{25}{8\pi^2} \frac{\lambda^2}{t_f^2} \frac{1}{|\beta_f - \beta_b|^2} \exp(\mu_b t_b) \quad (38)$$

$$\bar{n}_{\text{zpc}} = \frac{25}{8\pi^2} \frac{\lambda^2}{t_f^2} \frac{1}{|\delta_f - \delta_b|^2} \exp(\mu_b t_b). \quad (39)$$

These expressions for the required number of photons per pixel scale with feature thickness as t_f^2 , while the area also decreases with t_f^2 if we assume an isotropic (cubic) specimen; thus we are consistent with other analyses [21, 8, 44] that arrive at a fourth power scaling between resolution improvements and required exposure.

4 X-ray microscopy: a more complete model

The above expressions are essentially what have been used in dose estimates in x-ray microscopy that update the early work of Sayre et al. [21, 22] by including phase contrast [24, 25]. However, they are simplified expressions that ignore potentially complicating effects beyond photoelectric absorption and simple refractive phase. We therefore wish to consider a more complete model.

4.1 X-ray normalized intensity categories

The probability P for individual photon interactions within a sample thickness dt is given by

$$P = \sigma_i \rho dt \quad (40)$$

where σ_i is the cross section for interaction event i , and ρ is the sample density. The interaction events i we now want to consider are photoelectric absorption as before ($i \rightarrow \text{abs}$), elastic or Rayleigh scattering ($i \rightarrow \text{el}$), and inelastic (Compton) scattering ($i \rightarrow \text{inel}$). These cross sections are well tabulated [62, 63, 56] and are available in the subroutine library `xraylib` [57] which we have used for our calculations. With these tabulated data in hand, we can simplify the algebra that follows by writing the various interaction coefficients per sample thickness dt from Eq. 40 as

$$K_{\text{el}} = \sigma_{\text{el}} \rho \quad (41)$$

$$K_{\text{inel}} = \sigma_{\text{inel}} \rho \quad (42)$$

$$K_{\text{el},\text{in}} = \sigma_{\text{el}}(1 - \eta_{\text{el}})\rho \quad (43)$$

$$K_{\text{inel},\text{in}} = \sigma_{\text{inel}}(1 - \eta_{\text{inel}})\rho \quad (44)$$

$$K_{\text{out}} = \sigma_{\text{el}}\eta_{\text{el}}\rho + \sigma_{\text{inel}}\eta_{\text{inel}}\rho \quad (45)$$

$$K_{\text{abs}} = \sigma_{\text{abs}}\rho \quad (46)$$

where η_{el} and η_{inel} are the probabilities that a photon is scattered more than 90° (that is, backscattered and thus lost to the imaging system) in an elastic and inelastic scattering event, respectively. The two fractions can be found [39] by integrating their corresponding differential cross sections over the forward direction ($\theta \leq 90^\circ$) to obtain

$$\sigma_{\text{el}} = \int_0^{\pi/2} [F(\theta/\lambda)]^2 \frac{r_e^2}{2} (1 + \cos^2 \theta) d\theta \quad (47)$$

$$\sigma_{\text{inel}} = \int_0^{\pi/2} [S(\theta/\lambda)]^2 \frac{r_e^2}{2} [1 + k(1 - \cos \theta)]^{-2} \left[1 + \cos^2 \theta + \frac{k^2(1 - \cos \theta)^2}{1 + k(1 - \cos \theta)} \right] d\theta \quad (48)$$

where Eq. 47 integrates the differential Thomson cross section for unpolarized radiation and the atomic form factor $F(\theta/\lambda, Z)$, while Eq. 48 integrates the Klein-Nishina cross section for the relative incident energy $k = E/m_e c^2$ and uses the incoherent scattering form factor $S(\theta/\lambda, Z)$. One can obtain numerical values for both σ_{el} and σ_{inel} by numerical integration of the respective formulae as tabulated in the subroutine library xraylib [57].

With the above, we can now follow the example of calculations in electron [33] and x-ray [26] microscopy to consider a more complete set of categories to which individual x-ray photons can “join” or “leave” depending on the respective interaction cross sections:

- **Unscattered:** all photons are in this category at the outset, but they leave according to

$$dI_{\text{noscat}} = -I_{\text{noscat}}(K_{\text{inel}} + K_{\text{el}} + K_{\text{abs}})dt. \quad (49)$$

The initial condition is $I_{\text{noscat}}(0) = I_0$.

- **Single elastic scattered:** unscattered photons can enter this category, while photons leave this category due to various scattering events giving

$$dI_{\text{1el}} = I_{\text{noscat}}K_{\text{el,in}}dt - I_{\text{1el}}(K_{\text{inel}} + K_{\text{el}} + K_{\text{abs}})dt \quad (50)$$

with $I_{\text{1el}}(0) = 0$.

- **Detected plural scattered:** photons undergoing multiple elastic scattering events while remaining within the detectable aperture are described by

$$dI_{\text{el,plural}} = I_{\text{1el}}K_{\text{el,in}}dt - I_{\text{el,plural}}(K_{\text{out}} + K_{\text{inel,in}} + K_{\text{abs}})dt \quad (51)$$

with $I_{\text{el,plural}}(0) = 0$.

- **Backscattered:** photons that are scattered out of the detectable angular range (whether due to elastic, or inelastic, scattering) are given by

$$dI_{\text{out}} = (I_0 - I_{\text{out}} - I_{\text{abs}})K_{\text{out}}dt \quad (52)$$

with $I_{\text{out}}(0) = 0$.

- **Absorbed:** photons from any of the forward-directed ~~category~~ [categories](#) can always be absorbed according to

$$dI_{\text{abs}} = (I_0 - I_{\text{out}} - I_{\text{abs}})K_{\text{abs}}dt \quad (53)$$

with $I_{\text{abs}}(0) = 0$.

- **Not inelastic scattered:** the fraction of detectable photons that have not undergone inelastic scattering (the sum $I_{\text{noscat}} + I_{\text{1el}} + I_{\text{el,plural}}$) is denoted as $I_{\text{in,noinel}}$ and given by

$$dI_{\text{in,noinel}} = -I_{\text{in,noinel}}(K_{\text{inel,in}} + K_{\text{out}} + K_{\text{abs}}) \quad (54)$$

with $I_{\text{in,noinel}}(0) = 0$.

- **Inelastically scattered within aperture:** the fraction of photons that undergo at least one inelastic scattering yet are still within the detectable aperture is given by

$$dI_{\text{inel}} = I_{\text{in,noinel}}K_{\text{inel}}dt - I_{\text{inel}}(K_{\text{out}} + K_{\text{abs}})dt \quad (55)$$

with $I_{\text{inel}}(0) = 0$.

Solving these coupled differential equations yields

$$\text{Unscattered: } I_{\text{noscat}} = I_0 e^{-(K_{\text{inel}} + K_{\text{el}} + K_{\text{abs}})t} \quad (56)$$

$$\begin{aligned} \text{Single elastic scattered: } I_{\text{1el}} &= I_0 K_{\text{el, in}} e^{-(K_{\text{inel}} + K_{\text{el}} + K_{\text{abs}})t} \\ &= K_{\text{el, in}} t I_{\text{noscat}} \end{aligned} \quad (57)$$

$$\begin{aligned} \text{Plural scattered: } I_{\text{el, plural}} &= I_0 \left[e^{-(K_{\text{out}} + K_{\text{inel, in}} + K_{\text{abs}})t} - \right. \\ &\quad \left. (1 + K_{\text{el, in}} t) e^{-(K_{\text{inel}} + K_{\text{el}} + K_{\text{abs}})t} \right] \end{aligned} \quad (58)$$

$$\text{Scattered out: } I_{\text{out}} = \frac{I_0 K_{\text{out}}}{K_{\text{out}} + K_{\text{abs}}} \left[1 - \exp[-(K_{\text{out}} + K_{\text{abs}})t] \right] \quad (59)$$

$$\text{Absorbed: } I_{\text{abs}} = \frac{I_0 K_{\text{abs}}}{K_{\text{out}} + K_{\text{abs}}} \left[1 - \exp[-(K_{\text{out}} + K_{\text{abs}})t] \right] \quad (60)$$

$$\text{Scattered in, no inelastic: } I_{\text{in, noinel}} = I_0 \exp[-(K_{\text{inel, in}} + K_{\text{out}} + K_{\text{abs}})t] \quad (61)$$

$$\begin{aligned} \text{Inelastic scattered: } I_{\text{inel}} &= I_0 \left[\exp[-(K_{\text{out}} + K_{\text{abs}})t] - \right. \\ &\quad \left. \exp[-(K_{\text{inel, in}} + K_{\text{out}} + K_{\text{abs}})t] \right] \end{aligned} \quad (62)$$

and it can be confirmed that the above expressions satisfy

$$I_{\text{noscat}} + I_{\text{1el}} + I_{\text{el, plural}} + I_{\text{out}} + I_{\text{abs}} + I_{\text{inel}} = I_0 \quad (63)$$

as expected. For a generic protein feature lying in amorphous ice and EPON resin matrices, the expressions of Eqs. 56–62 are plotted in Figs. 2 and 3 as a function of overall background material thickness for three example x-ray energies: 5, 15, and 45 keV.

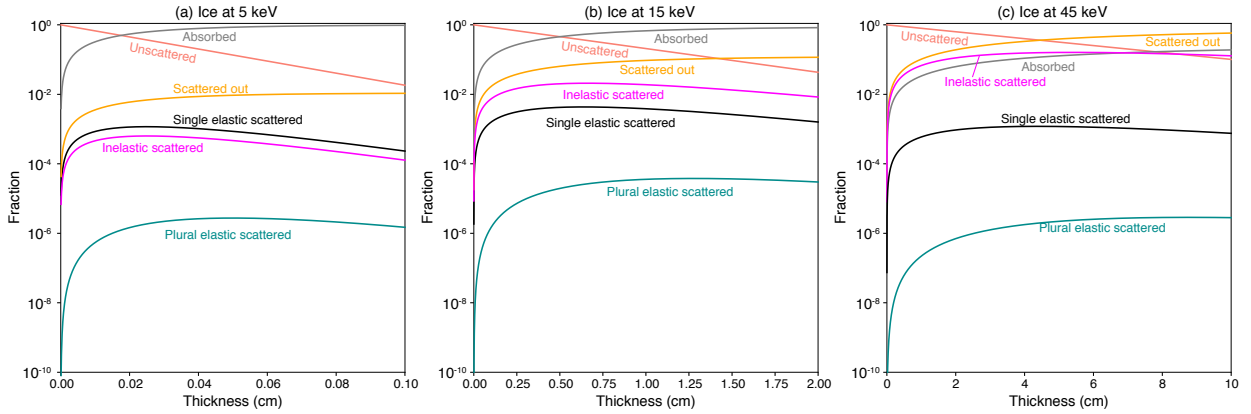


Figure 2: Normalized intensity fractions for x-rays in amorphous ice as a function of thickness at incident photon energies of (a) 5 keV, (b) 15 keV, and (c) 45 keV. Phase contrast imaging involves an interference between unscattered (I_{noscat} ; Eq. 56) and single elastically scattered (I_{1el} ; Eq. 58) photons, with other intensity fractions representing signal loss or background (these are described in Eqs. 58–62). The corresponding intensity fractions for the embedding medium EPON are shown in Fig. 3.

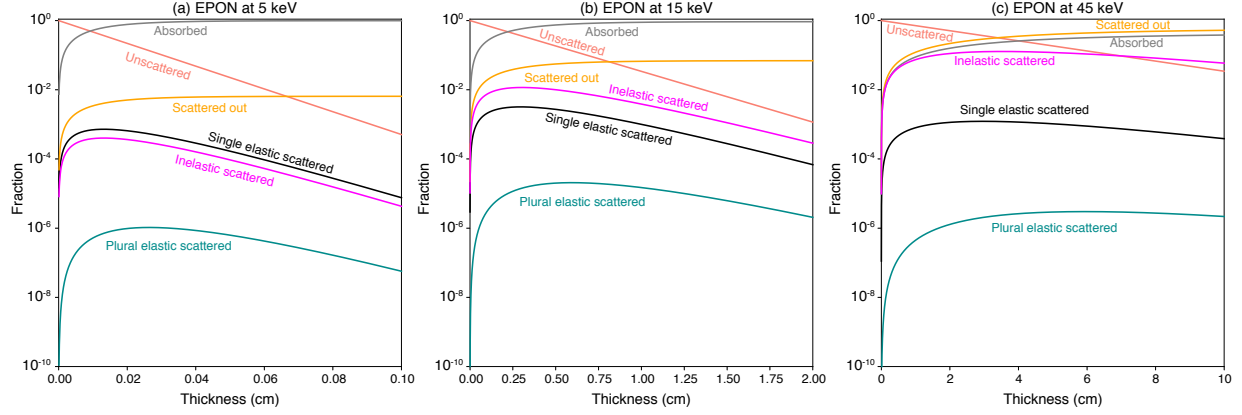


Figure 3: Normalized intensity fractions for x-ray in EPON as a function of thickness at incident photon energies of (a) 5 keV, (b) 15 keV, and (c) 45 keV. The corresponding intensity fractions for amorphous ice (such as for frozen hydrated specimens viewed under cryogenic conditions) are shown in Fig. 2.

4.2 Continuous versus atomistic features

The above analyses can be used to evaluate the quality and statistical quantities of the acquired images only if the continuous specimen assumption remains valid. This requires that neither the background or feature material has optically significant structure at length scales smaller than t_f , the spatial resolution of the imaging experiment. If that is the case, then there is a coherent superposition of scattering amplitudes within the numerical aperture of the imaging experiment from structures within the resolution scale t_f . This is in fact a condition assumed by the previous imaging-based analyses cited earlier. If instead there is significant structure within a pixel, one might have to consider the fraction of signal scattered to angles beyond the numerical aperture (NA) of the imaging system; that is, one would have a reduction in intensities I_{el} , $I_{\text{el,plural}}$, and I_{inel} . Obviously this approximation becomes increasingly invalid as the resolution t_f is decreased down towards values where there are a small number of molecules within a distance t_f so that the feature begins to look “lumpy” and scatters into larger angles. As an example, one simulation study of gold atoms in amorphous and crystalline particles indicated that this approximation becomes invalid at length scales of about 1 nm [64].

To understand the limits where atomic structure begins to produce significant scattering beyond the acceptance of an experiment with a limiting numerical aperture corresponding to the resolution t_f in biologically-significant materials, we turned to small angle x-ray scattering (SAXS) data of 80 different protein samples retrieved from Small Angle Scattering Biological Data Bank (SASBDB) [65]. Data parameterization is done among all data retrieved to yield a representative scattering distribution $I(s)$ of

$$\log_{10} I(s) = 0.007466s^5 - 0.1068s^4 + 0.5305s^3 - 0.8888s^2 - 0.6426s + 0.08601 \quad (64)$$

where

$$s = 4\pi \frac{\sin(\theta)}{\lambda} \quad (65)$$

is the momentum transfer of scattering (in nm^{-1} for the parameterization of Eq. 64), with 2θ as the scattering angle. While it is usual to denote momentum transfer with q in the x-ray scattering literature, we use s for consistency with electron microscopy calculations [33]. From Eq. 64, we can obtain an expectation value for s of

$$\langle s \rangle = \frac{\int_0^\infty s I(s) ds}{\int_0^\infty I(s) ds} \approx 0.42 \text{ nm}^{-1}. \quad (66)$$

If we assume the value of the numerical aperture exactly matches $\langle s \rangle$, then the fraction f_{NA} of photons scattered into the aperture can be found through

$$f_{\text{NA}} = \frac{\int_0^{\langle s \rangle} I(s) ds}{\int_0^\infty I(s) ds} \approx 0.66. \quad (67)$$

That is, approximately 66% of the photons are accepted within a square (rather than circular) numerical aperture if the imaging system were to collect signal from a square of width $\Delta = 0.5\lambda/\text{NA}$ with NA replaced by $\langle s \rangle = 0.42 \text{ nm}^{-1}$ (that is, a square pixel resolution of $\Delta = 7.40 \text{ nm}$ using 5 keV x-rays). In other words, when the square pixel feature size t_f decreases towards a value of 7.40 nm, one would want account for f_{NA} in the expressions for I_{1el} , $I_{\text{el,plural}}$, and I_{inel} ; however, we will not apply the corrective factor f_{NA} in the calculations that follow.

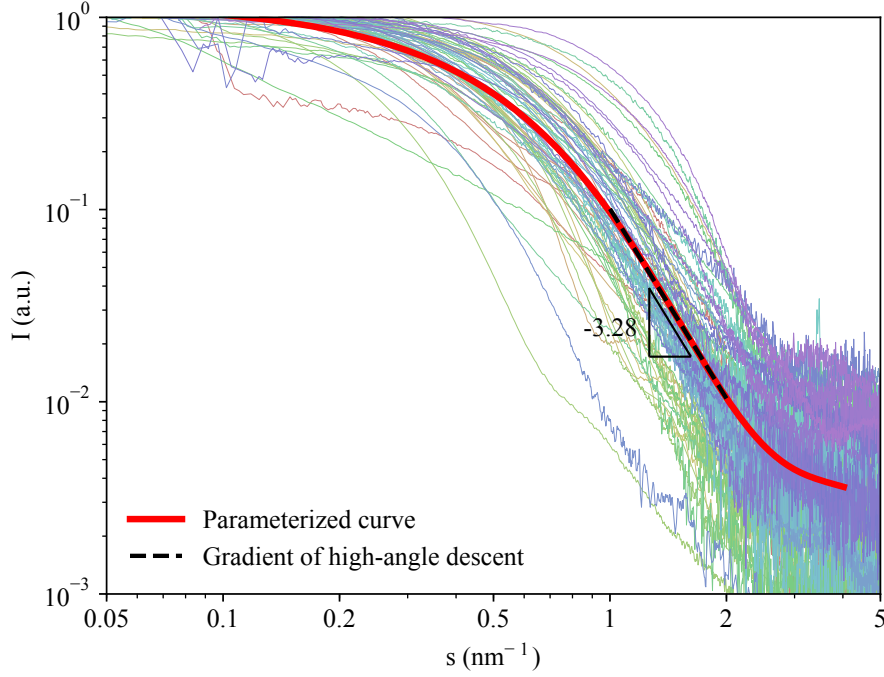


Figure 4: The approximation of structure being continuous at length scales finer than the spatial resolution t_f begins to break down when molecular scattering exceeds the corresponding numerical aperture. Shown here as a series of thin lines are the small angle scattering patterns $I(s)$ from 80 different macromolecules in small angle scattering patterns in SASBDB, the Small Angle Scattering Biological Data Bank [65]. To obtain a single parameterized representation of these patterns versus momentum transfer s , a sixth-order polynomial fit of $\log_{10}[I(s)]$ was obtained, leading to the expression of Eq. 64. This parameterized fit is shown as the thick red line.

4.3 X-ray imaging intensities for thicker specimens

Having determined the normalized intensities of x-rays in various interaction categories, we can carry out a more complete calculation of image signals with, and without, features present. Starting from Eqs. 56–62,

we arrive at expressions for the background or feature-absent case of

$$I_{\text{nosc},b} = I_0 \exp[-(K_{\text{inel},b} + K_{\text{el},b} + K_{\text{abs},b})t] \quad (68)$$

$$\begin{aligned} I_{\text{el},b} &= I_0 K_{\text{el},\text{in},b} \exp[-(K_{\text{inel},b} + K_{\text{el},b} + K_{\text{abs},b})t] \\ &= K_{\text{el},\text{in},b} t I_{\text{nosc},b} \end{aligned} \quad (69)$$

$$I_{\text{in},\text{noinel},b} = I_0 \exp[-(K_{\text{inel},\text{in},b} + K_{\text{out},b} + K_{\text{abs},b})t] \quad (70)$$

$$I_{\text{el},\text{plural},b} = I_{\text{in},\text{noinel},b} - I_{\text{nosc},b} - I_{\text{el},b} \quad (71)$$

$$I_{\text{out},b} = \frac{I_0 K_{\text{out},b}}{K_{\text{out},b} + K_{\text{abs},b}} \left(1 - \exp[-(K_{\text{out},b} + K_{\text{abs},b})t]\right) \quad (72)$$

$$I_{\text{abs},b} = \frac{I_0 K_{\text{abs},b}}{K_{\text{out},b} + K_{\text{abs},b}} \left(1 - \exp[-(K_{\text{out},b} + K_{\text{abs},b})t]\right) \quad (73)$$

$$I_{\text{inel},b} = I_0 - I_{\text{out},b} - I_{\text{abs},b} - I_{\text{in},\text{noinel},b} \quad (74)$$

whereas the feature-present case is described by [equations including](#)

$$I_{\text{nosc},f} = I_0 \exp[-(K_{\text{inel},b} + K_{\text{el},b} + K_{\text{abs},b})t_b] \exp[-(K_{\text{inel},f} + K_{\text{el},f} + K_{\text{abs},f})t_f] \quad (75)$$

$$I_{\text{el},f} = (K_{\text{el},\text{in},b} t_b + K_{\text{el},\text{in},f} t_f) I_{\text{nosc},f} \quad (76)$$

$$I_{\text{el},f/f} = K_{\text{el},\text{in},f} t_f I_{\text{nosc},f} \quad (77)$$

$$I_{\text{in},\text{noinel},f} = I_0 \exp[-(K_{\text{out},b} + K_{\text{inel},\text{in},b} + K_{\text{abs},b})t_b] \exp[-(K_{\text{out},f} + K_{\text{inel},\text{in},f} + K_{\text{abs},f})t_f] \quad (78)$$

$$I_{\text{el},\text{plural},f} = I_{\text{in},\text{noinel},f} - I_{\text{nosc},f} - I_{\text{el},f}. \quad (79)$$

The signal from the feature slice is gradually reduced in downstream layers due to scattering. This is described by $I_{\text{out}/f,f}$ and $I_{\text{abs}/f,f}$, which are formulated in a fashion similar to Eqs. 72 and 73. The differences within the feature slice are that the interaction coefficients (the K coefficients) of the background material are replaced by those of the feature, and t is changed to t_f . In addition, the incident intensity I_0 in Eqs. 72 and 73 is replaced by $I_0 - I_{\text{out},b}(t_b/2) - I_{\text{abs},b}(t_b/2)$, which is the intensity that remains after absorption and out-of-aperture scattering in the overlying slab (the “incident intensity” at the upper boundary of the feature slice):

$$I_{\text{out}/f,f} = \frac{[I_0 - I_{\text{out},b}(t_b/2) - I_{\text{abs},b}(t_b/2)] K_{\text{out},f}}{K_{\text{out},f} + K_{\text{abs},f}} \left(1 - \exp[-(K_{\text{out},f} + K_{\text{abs},f})t_f]\right) \quad (80)$$

$$I_{\text{abs}/f,f} = \frac{[I_0 - I_{\text{out},b}(t_b/2) - I_{\text{abs},b}(t_b/2)] K_{\text{abs},f}}{K_{\text{out},f} + K_{\text{abs},f}} \left(1 - \exp[-(K_{\text{out},f} + K_{\text{abs},f})t_f]\right). \quad (81)$$

Based on these, the total signal scattered outside the aperture of the detector is given by

$$\begin{aligned} I_{\text{out},f} &= I_{\text{out},b}(t_b/2) + I_{\text{out}/f,f} + \\ &\quad \frac{I_0 - I_{\text{out},b}(t_b/2) - I_{\text{abs},b}(t_b/2) - I_{\text{out}/f,f} - I_{\text{abs}/f,f}}{I_0} I_{\text{out},b}(t_b/2) \end{aligned} \quad (82a)$$

The equation consists of three terms, describing the amount of photons scattered out in the overlying background material, out of the feature slice in the middle, and out of the underlying background material. Following the definition in Eq. 72, $I_{\text{out},b}(t_b/2)$ gives the amount of photons scattered out in the background material of thickness $t_b/2$, given an incident intensity of I_0 , which is the thickness of the overlying slab. Within the feature slice at the middle, the amount of photons scattered out is $I_{\text{out}/f,f}$. The third term is the amount of out-of-aperture photons contributed by the underlying slab, but the incident intensity I_0 in $I_{\text{out},b}(t_b/2)$ has to be replaced by the beam intensity after being attenuated by the overlying and middle slab, which is accounted for by the prefactor of $I_{\text{out},b}(t_b/2)$. For $t_f \ll t_b$, the first and third terms in the equation can be collectively replaced by $I_{\text{out},b}(t_b)$, resulting in

$$I_{\text{out},f} \simeq I_{\text{out},b}(t_b) + I_{\text{out}/f,f}. \quad (82b)$$

This approximation is based on the assumption that the attenuation caused in the middle slice does not significantly alter the beam intensity at the upper boundary of the underlying material. Along with similar

considerations for photoelectric absorption, we arrive at

$$I_{\text{abs},f} = I_{\text{abs},b}(t_b/2) + I_{\text{abs}/f,f} + \frac{I_0 - I_{\text{out},b}(t_b/2) - I_{\text{abs},b}(t_b/2) - I_{\text{out}/f,f} - I_{\text{abs}/f,f}}{I_0} I_{\text{abs},b}(t_b/2) \quad (82c)$$

where the approximation at $t_f \ll t_b$ similarly applies to Eq. 82c. Finally, this set of equations are completed by the expression

$$I_{\text{inel}} = I_0 - I_{\text{out},f} - I_{\text{abs},f} - I_{\text{in,noinel},f}. \quad (82d)$$

These intensities are dominated by interactions in the background material as shown in Figs. 2 and 3, except for the crucial differences caused by feature material being present or absent in the region of width and thickness t_f .

Now that we are considering the case where $I_{\text{el},\text{plural}}$, I_{inel} , and I_{out} have non-negligible contributions, they have to be incorporated into Θ . We do so by returning to the feature-containing A_f (Eq. 25) and feature-absent A_b (Eq. 26) amplitudes in Zernike phase contrast. These amplitudes included a reduction $I_0[1 - I_{\text{abs},i}(t)]$ of the wavefield incident upon the imaged pixel, but now the amplitudes are further reduced by the presence of these additional scattering terms. This means that these amplitudes must be reduced further according to a correction term $C_i(t)$ of

$$C_i(t) = \frac{I_0 - I_{\text{abs},i}(t) - I_{\text{el},\text{plural},i}(t) - I_{\text{inel},i}(t) - I_{\text{out}}(t)}{I_0 - I_{\text{abs},i}(t)} \quad (83)$$

where t again represents the total specimen thickness. The modified wave amplitudes corresponding to Eqs. 25 and 26 then become

$$A_f = A_0 \exp[-(\mu_b/2)t_b] \exp[i\eta_b t_b] \exp[-(\mu_f/2)t_f] \exp[i\eta_f t_f] \sqrt{C_b(t_b)C_f(t_f)} \quad (84)$$

$$A_b = A_0 \exp[-(\mu_b/2)t_b] \exp[i\eta_b t_b] \exp[-(\mu_b/2)t_f] \exp[i\eta_b t_f] \sqrt{C_b(t_b)C_b(t_f)} \quad (85)$$

where A_0 is the amplitude of the incident beam. If we neglect absorption in the phase ring used in Zernike phase contrast so that it only applies a phase shift $\exp[i\phi]$, the image intensity equivalents to Eqs. 31 and 32 become

$$I_{\text{signal},f} = I_0 \exp(-\mu_b t_b) C_b(t_b) \left\{ 2 \left[\cos[\phi + (\eta_b - \eta_f)t_f] - \cos[(\eta_b - \eta_f)t_f] \right] \times \right. \\ \left. \exp[-(\mu_b + \mu_f)t_f/2] \sqrt{C_b(t_f)C_f(t_f)} + \right. \\ \left. (2 - 2 \cos \phi) \exp(-\mu_b t_f) C_b(t_f) + \exp(-\mu_f t_f) C_f(t_f) \right\} \quad (86)$$

$$I_{\text{signal},b} = I_0 \exp(-\mu_b t) C_b(t_b) C_b(t_f) \quad (87)$$

For an ideal phase ring with $\phi = \pi/2$, and the limiting case that the amplitude correction terms $C_i(t)$ become 1, Eqs. 86 and 87 reduce to Eqs. 31 and 32. If instead we “turn off” the phase ring by setting $\phi = 0$ while also working in the thin specimen limit with $C_i(t) \rightarrow 1$, it can be shown that Eqs. 86 and 87 reproduce the thin specimen limit expressions for absorption contrast of Eqs. 18 and 19. Thus the intensities of Eqs. 86 and 87 can be used to describe both absorption ($\phi = 0$) and Zernike phase contrast ($\phi = \pi/2$) for thick specimens with the effects of $I_{\text{el},\text{plural}}$, I_{inel} , and I_{out} included. In this case the contrast parameter Θ is modified from the expressions of Eqs. 21 or 35 to become

$$\Theta = \frac{|I_{\text{signal},f} - I_{\text{signal},b}|}{\sqrt{I_{\text{noise},f} + I_{\text{noise},b}}}. \quad (88)$$

using Eqs. 86 and 87, as well as an expression for the background signals of

$$I_{\text{noise},i} = I_{\text{signal},i} + I_{\text{inel},i} + I_{\text{el},\text{plural},i}. \quad (89)$$

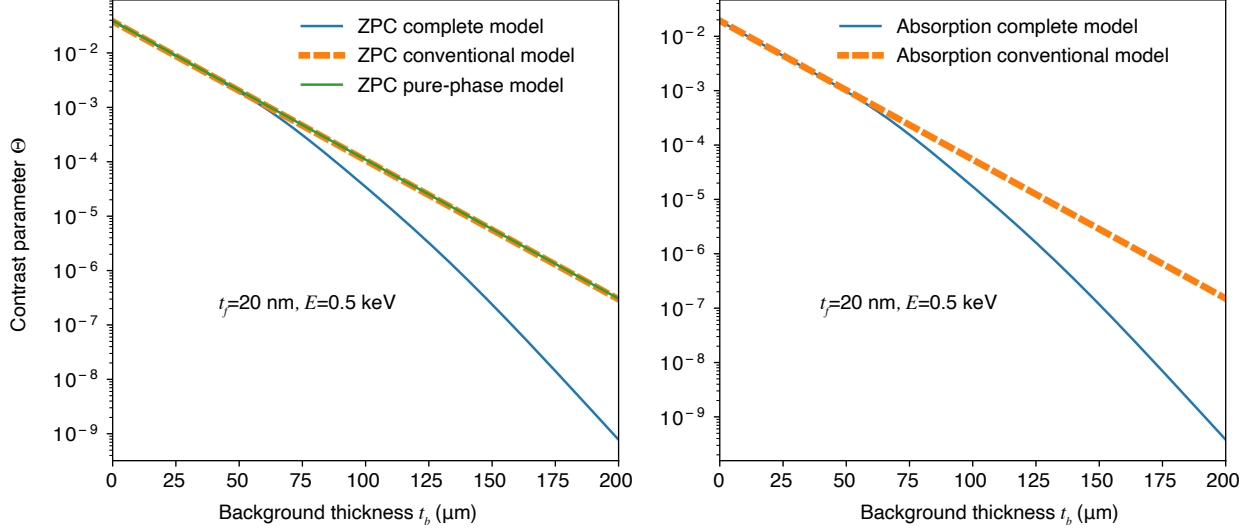


Figure 5: Contrast parameter Θ for soft x-ray (0.5 keV) imaging of $t_f = 20$ nm protein features as a function of amorphous ice thicknesses t_b . At left is shown the case for Zernike phase contrast using the pure-phase thin sample approximation of Eq. 36, the conventional model of Eq. 35, and the complete model of Eq. 88 with phase contrast ($\phi = \pi/2$). The discrepancy between the pure-phase thin sample approximation and the conventional model is due to the fact that there is significant absorption at the soft x-ray energy of 0.5 keV, even though this is within the “water window” spectral region between the carbon (0.290 keV) and oxygen (0.540 keV) x-ray absorption edges.

Because the plural elastic and inelastic terms do not carry structural information, they only contribute to the noise term in the denominator of Eq. 88.

As summarized in Table 1, we have arrived at three ways to express the contrast parameter Θ for absorption and phase contrast in x-ray microscopy: in the simplest thin specimen limit (Eqs. 23 and 37), in a form for thicker specimens as has been described previously (Eqs. 21 and 35), and in a complete form that includes for the first time the effects of inelastic and plural elastic scattering (Eq. 88). When do these expressions differ in significant ways? Some insight can be provided by the relative intensities shown in Figs. 2 and 3, where it is clear that that I_{noscat} and I_{1el} are orders of magnitude larger than the background signals I_{inel} and $I_{\text{el,plural}}$ even if most of the incident beam has been absorbed. This means that even when the incident illumination is greatly attenuated, the remaining imaging signal is still quite “clean” with relatively little signal contamination. This is why X rays are so successful at imaging very thick specimens, even up to entire organisms.

In order to see this more clearly, we show in Figs. 5–7 the contrast parameter Θ calculated for different x-ray energies, imaging conditions, and specimen and background thicknesses. The case of Zernike phase and absorption contrast for soft x-ray microscopy is shown in Fig. 5, illustrating the fact that the pure-phase approximation used in Eqs. 36 and 37 is inaccurate in the soft x-ray range due to its exclusion of absorption contrast effects. When using hard x-rays (15 keV in this example), protein features in ice show almost no absorption contrast so in Fig. 6 we show Zernike phase contrast only for fine features ($t_f = 20$ nm) as well as for thicker features ($t_f = 1000$ nm) in ice thicknesses up to 1 mm. As can be seen, the conventional model of Eq. 35 works well for very thin features in thin ice layers, but as the overall specimen thickness becomes larger than tens of micrometers and/or the feature size approaches 1 μm , one must use the complete expression of Eq. 88 with $\phi = \pi/2$. In other words, inelastic and plural elastic scattering affect image contrast (and therefore required exposure and dose) for micrometer-scale features as well as for overall specimen thicknesses of tens of micrometers and above.

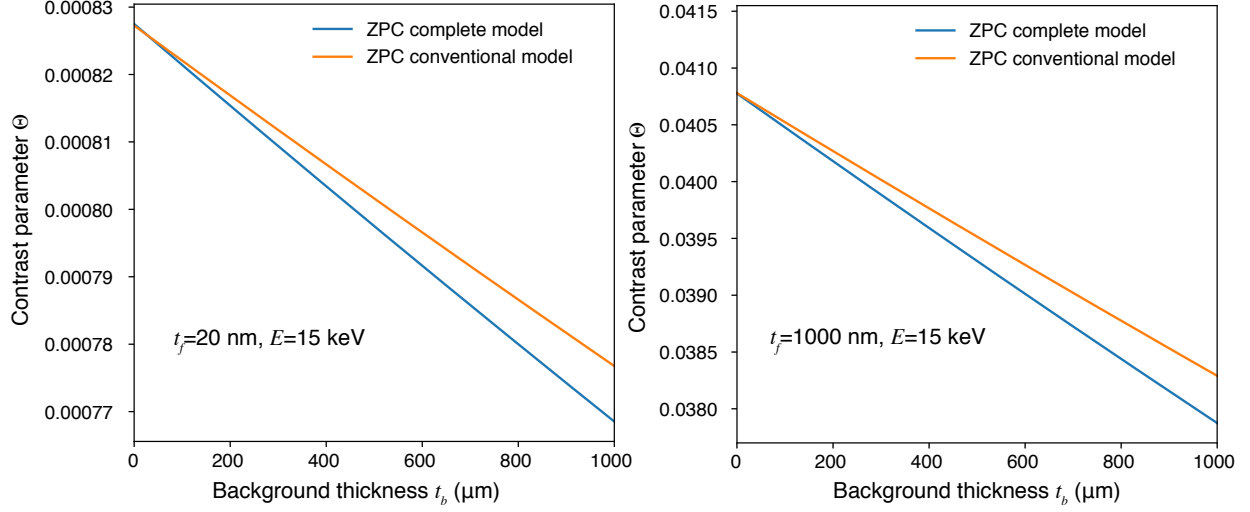


Figure 6: Contrast parameter Θ for Zernike phase contrast imaging with hard x-rays (15 keV) as a function of overall amorphous ice thickness. The case for a small protein feature ($t_f = 20$ nm) is shown at left, while the case for a larger protein feature ($t_f = 1000$ nm) is shown at right. The conventional Zernike phase contrast model of Eq. 35 works well for describing fine features in ice layers up to tens of micrometers thick, but the more complete model of Eq. 88 with phase contrast ($\phi = \pi/2$) becomes necessary with thicker features and ice layers. Absorption contrast is not shown because it is quite weak for hard x-ray imaging of organic materials in ice.

5 X-ray imaging absorbed dose

Once the appropriate expression for the contrast parameter Θ has been evaluated, one can arrive at the required number of photons per pixel \bar{n} using Eq. 8. This provide us with the basis of estimating the radiation dose, which is the energy deposited per mass. Accounting for attenuation by the overlying background material shown in Fig. 1, the flux per area incident upon the feature is given by $\bar{n} \exp(-\mu_b t_{b,o})$. The energy deposited per length dE/dx can be found from Eq. 15 as

$$\frac{dE}{dx} = \bar{n} \frac{hc}{\lambda} \frac{dI}{dx} = \bar{n} \frac{hc}{\lambda} \mu \quad (90)$$

where $E = hc/\lambda$ is the photon energy based on Planck's constant h and the speed of light c . Since this is incident on a feature with area Δ^2 and density ρ_f , this leads to a dose D_f absorbed in the feature of

$$D_f = \bar{n} \frac{hc}{\lambda} \frac{\mu_f}{\rho_f \Delta^2} \exp(-\mu_b t_{b,o}). \quad (91)$$

When the pixel width is equal to the feature thickness (or $\Delta = t_f$), this becomes

$$D_f = \bar{n} \frac{hc}{\lambda} \frac{\mu_f}{\rho_f t_f^2} \exp(-\mu_b t_{b,o}). \quad (92)$$

for the case of x-ray imaging of cubic features. Since the required number of incident photons \bar{n} is found from the contrast parameter Θ according Eq. 8, we arrive at a dose to the feature of

$$D_f = \frac{SNR^2}{\Theta^2} \frac{hc}{\lambda} \frac{\mu_f}{\rho_f t_f^2} \exp(-\mu_b t_{b,o}) \quad (93)$$

where setting $SNR=5$ corresponds to the Rose criterion [50]. In the thin specimen limits of Eqs. 23 and 37, and with the use of the Rose criterion, one can alternatively write the dose for absorption and phase contrast

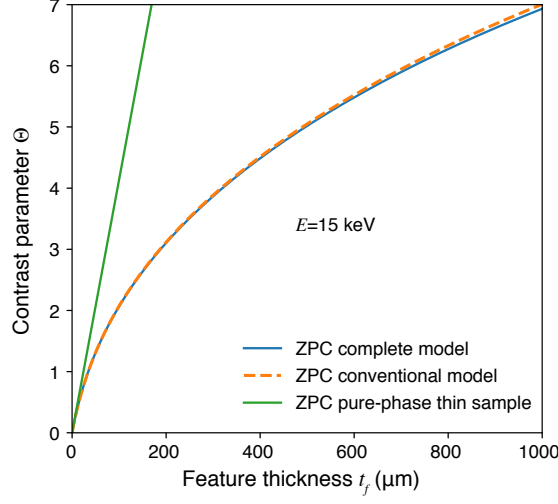


Figure 7: Contrast parameter Θ for Zernike phase contrast imaging with hard x-rays (15 keV) as a function of feature thickness t_f for protein in amorphous ice. In this case no overlying or underlying thickness was assumed (that is, $t_{b,o} = t_{b,u} = 0$ in Fig. 1), so this is just for a protein feature of the indicated thickness in an equal thickness slab of ice. As can be seen, the pure-phase thin sample expression of Eq. 36 gives inaccurate predictions for ice thicknesses of even a few tens of micrometers; the conventional model of Eq. 35 works well for thicknesses up to several hundreds of micrometers at which point the more complete expression of Eq. 88 with $\phi = \pi/2$ gives correct results.

in terms of the refractive index $n = 1 - \delta - i\beta$ as

$$D_{\text{abs}} \simeq SNR^2 \frac{hc}{2\pi\rho_f t_f^4} \frac{\beta_f}{|\beta_f - \beta_b|^2} \exp(\mu_b t_{b,u}) \quad (94)$$

$$D_{\text{zpc}} \simeq SNR^2 \frac{hc}{2\pi\rho_f t_f^4} \frac{\beta_f}{|\delta_f - \delta_b|^2} \exp(\mu_b t_{b,u}) \quad (95)$$

which again shows that the required radiation dose D increases with the fourth power of improvements in spatial resolution t_f . If one instead uses $\delta = \alpha\lambda^2 f_1$ and $\beta = \alpha\lambda^2 f_2$ from Eq. 13, the phase contrast expression becomes

$$D_f \approx SNR^2 \frac{hc}{2\pi\alpha\rho_f} \frac{1}{t_f^4} \frac{1}{\lambda^2} \frac{f_{2,f}}{|f_{1,f} - f_{1,b}|^2} \exp(\mu_b t_{b,u}). \quad (96)$$

At x-ray energies in the keV range, f_1 tends to approach a constant value of the atomic number Z for the element in question while f_2 scales like λ^2 [55]. Thus the decrease in D_f due to f_2 nearly exactly cancels out the increase in D_f due to the $1/\lambda^2$ term in Eq. 96. As a result, once absorption in the over- and underlying background material becomes negligible, the required dose shows very little dependence on the x-ray energy used; this will become apparent in Figs. 12 and 14. The required fluence $\bar{n} = SNR^2/\Theta^2$, however, will increase at higher x-ray energies due to decreases in the contrast parameter Θ .

6 Image contrast and dose in electron microscopy

Transmission electron microscopy has a long and enormously successful history in biological imaging, so it is useful to perform a similar analysis of its characteristics. In fact, several analytical analyses exist (as noted Sec. 1), but some of them ignore defocus phase contrast [21] while others [33, 32] do not carry their estimates through to the point of considering defocus phase contrast image intensities with feature present and absent as needed for the contrast parameter Θ in Eq. 7.

6.1 Electron cross sections

While electrons undergo both atomic scattering and a refractive-index-like phase advance due to the inner potential [66, 67, 68], there is not a direct equivalent to the extensive tabulations available for the x-ray refractive index in all materials [55]. However, there are convenient parameterizations of the primary interaction coefficients [33] which we use below. These parameterizations include a fraction η_{el} of elastically scattered electrons which do not pass through the objective aperture of

$$\eta_{\text{el}} \approx 1 - \frac{s_0}{10}. \quad (97)$$

The cross section for elastic scattering σ_{el} is well approximated by

$$\sigma_{\text{el}} = \frac{1.4 \times 10^{-6} Z^{3/2}}{\beta^2} \left(1 - \frac{0.26Z}{137\beta} \right) \text{ nm}^2, \quad (98)$$

where Z is the atomic number and β is the velocity relative to the speed of light c given by

$$\beta^2 = 1 - \left(\frac{m_e c^2}{V_0 + m_e c^2} \right)^2 \quad (99)$$

for an electron of mass m_e accelerated over a voltage V_0 . The cross section for inelastic scattering σ_{inel} is approximated by

$$\sigma_{\text{inel}} = \frac{1.5 \times 10^{-6} Z^{1/2}}{\beta^2} \ln(2/\theta_c) \text{ nm}^2 \quad (100)$$

where

$$\theta_c = \frac{\langle \Delta E \rangle}{\beta^2 (V_0 + m_e c^2)} \quad (101)$$

with $\langle \Delta E \rangle$ representing the mean energy loss of electron in the media. As noted by Langmore and Smith, Eq. 100 gives erroneous results for hydrogen so instead one uses

$$\sigma_{\text{inel}, Z=1} = 8.8 \left(\frac{\beta_{80 \text{ kV}}}{\beta} \right)^2 \text{ nm}^2 \quad (102)$$

which scales empirical observations made at $V_0 = 80 \text{ kV}$. The value of η_{inel} (the fraction of inelastically scattered electrons blocked by the objective aperture) is assumed to be $\eta_{\text{inel}} = 0$ as inelastic electron scattering typically involves very small angles [69]; we will therefore ignore η_{inel} in what follows.

6.2 Mean energy loss $\langle \Delta E \rangle$

The expression for the inelastic cross section σ_{inel} requires knowledge of the mean energy loss $\langle \Delta E \rangle$ of electrons in a material, and this quantity is also needed for calculating the dose in electron microscopy (Eq. 131). This energy can be measured using electron energy loss spectroscopy (EELS) from a thin specimen. We have obtained EELS spectra for our two background materials: amorphous ice (based on 100 kV data provided by Richard Leapman, National Institutes of Health), and EPON (based on 80 kV data acquired with Kai He, using a sample prepared by Qiaoling Jin; both are with Northwestern University). From the as-recorded spectrum, one can calculate the single-inelastic-scatter spectrum $I_{\text{inel}}(\Delta E)$ using a Fourier-log deconvolution method [70, 71]. The raw EELS spectrum for amorphous ice, as well as the single-inelastic spectra for amorphous ice and for EPON, are shown shown in Fig. 8. From the single-inelastic-scatter spectrum $I_{\text{inel}}(\Delta E)$, one can calculate the mean energy loss $\langle \Delta E \rangle$ using

$$\langle \Delta E \rangle = \frac{\int_0^\infty (\Delta E) I_{\text{inel}}(\Delta E) d\Delta E}{\int_0^\infty I_{\text{inel}}(\Delta E) d\Delta E}. \quad (103)$$

The values we obtained for $\langle \Delta E \rangle$ are very similar between amorphous ice (39.3 eV) and EPON (38.6 eV), and these values are similar to earlier measurements showing $\langle \Delta E \rangle \simeq 37 \text{ eV}$ in nucleic acids [72, 73].

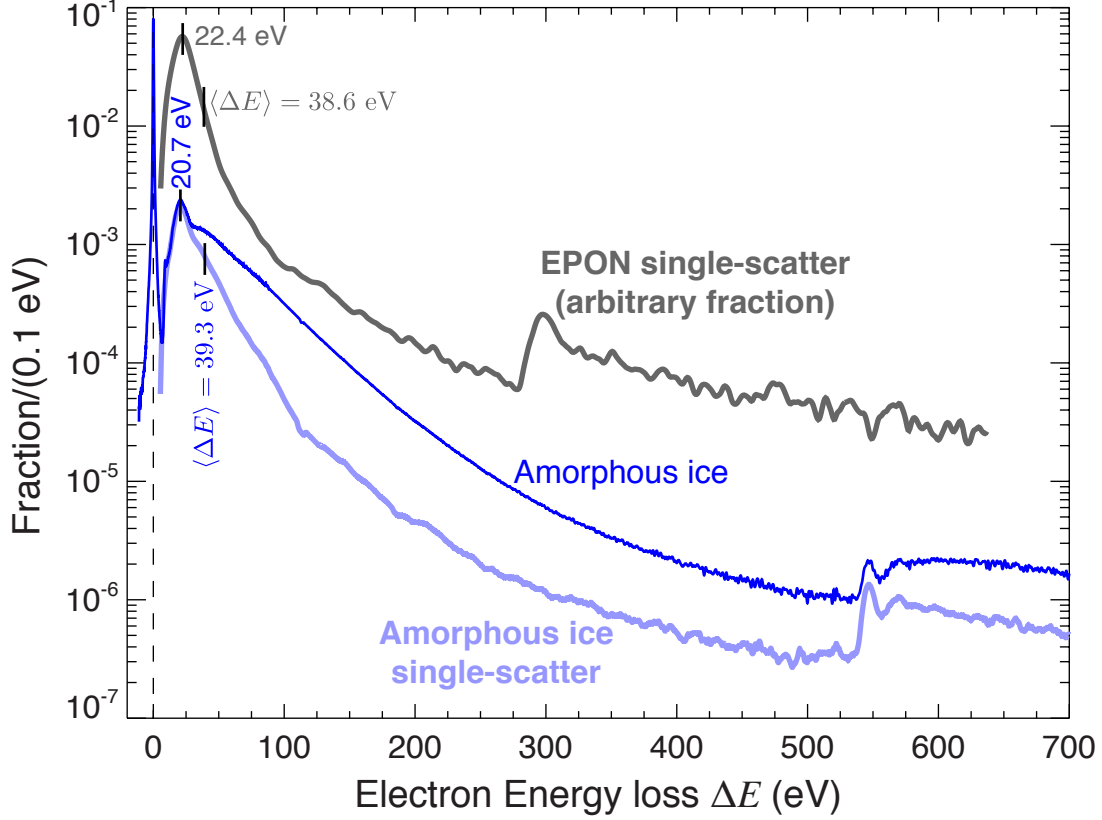


Figure 8: Electron Energy Loss Spectroscopy (EELS) of amorphous ice and of the plastic embedding medium EPON. The EPON EELS spectrum shows a increase at the carbon K edge at 290 eV, while the ice EELS spectrum shows an increase at the oxygen K edge at 540 eV. For amorphous ice, the as-recorded spectrum is shown along with the single-inelastic-scatter spectrum obtained by Fourier-log deconvolution; for EPON, only the single-inelastic-scatter spectrum is shown with arbitrary absolute scaling. Also shown are the locations of the plasmon mode peaks of the inelastic spectra, and the values of the mean energy loss $\langle \Delta E \rangle$ as calculated using Eq. 103. Amorphous ice spectra courtesy Richard Leapman, National Institutes for Health. The EPON spectra are from a sample prepared by Qiaoling Jin, with assistance on EELS spectrum recording provided by Kai He, both of Northwestern University.

6.3 Electron interaction probabilities

Having established functional forms for electron interaction cross sections in Sec. 6.1, we can proceed in a manner similar to that used for x-ray interactions in Sec. 4. We first write the interaction probability K for electrons to undergo elastic scattering as

$$K_{\text{el}} = \sigma_{\text{el}}\rho, \quad (104)$$

for those singly scattered inside and outside the acceptance of the objective respectively as

$$K_{\text{el},\text{in}} = \sigma_{\text{el}}(1 - \eta_{\text{el}})\rho \quad (105)$$

$$K_{\text{out}} = \sigma_{\text{el}}\eta_{\text{el}}\rho, \quad (106)$$

and for the probability for electrons to be singly inelastically scattered yet remain within the aperture as

$$K_{\text{inel},\text{in}} = \sigma_{\text{inel}}\rho = K_{\text{inel}}. \quad (107)$$

We can then assign electrons to categories [26] similar to those found in Eqs. 56–62 to obtain

$$\text{Unscattered: } I_{\text{noscat}} = I_0 e^{-(K_{\text{inel}} + K_{\text{el}})t} \quad (108)$$

$$\begin{aligned} \text{Single elastic scattered: } I_{\text{1el}} &= I_0 K_{\text{el, in}} e^{-(K_{\text{inel}} + K_{\text{el}})t} \\ &= K_{\text{el, in}} t I_{\text{noscat}} \end{aligned} \quad (109)$$

$$\text{Plural scattered: } I_{\text{el, plural}} = I_0 \left[e^{-(K_{\text{out}} + K_{\text{inel}})t} - (1 + K_{\text{el, in}} t) e^{-(K_{\text{inel}} + K_{\text{el}})t} \right] \quad (110)$$

$$\text{Scattered out : } I_{\text{out}} = I_0 (1 - e^{-K_{\text{out}} t}) \quad (111)$$

$$\text{Scattered in, no inelastic : } I_{\text{in, noinel}} = I_0 e^{-(K_{\text{inel}} + K_{\text{out}})t} \quad (112)$$

$$\text{Inelastic scattered: } I_{\text{inel}} = I_0 \left[e^{-K_{\text{out}} t} - e^{-(K_{\text{inel}} + K_{\text{out}})t} \right]. \quad (113)$$

These normalized intensities for electrons in amorphous ice and in EPON are shown in Figs. 9 and 10, respectively, for the frequently-used electron beam energies of 100 and 300 keV. These plots can be compared with the equivalents for x-rays shown in Figs. 2 and 3. As noted in Sec. 1.1, electron microscopy gives very strong interactions for thin materials with modest energy deposition per elastically scattered electron, but electrons have a much higher fraction of inelastic and plural elastic scattered electrons present when imaging even micrometer thick specimens; both of these signals can lead to a background “fog” when imaging thicker specimens. With x-rays, the fractions of these signals are much lower even for sample thicknesses of centimeters, leading to considerably less image “fog.”

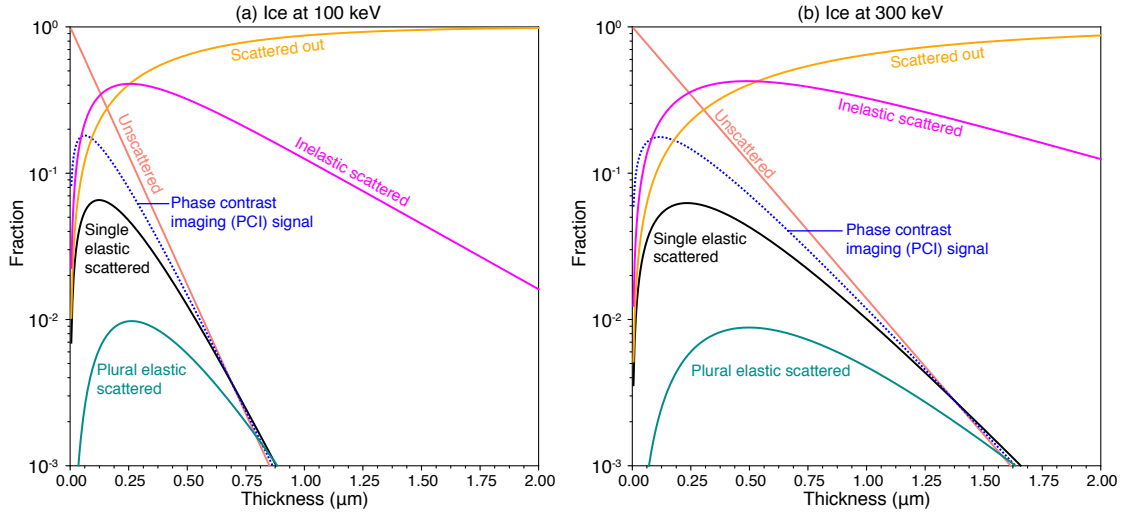


Figure 9: Normalized intensity profiles for phase contrast electron imaging in amorphous ice as a function of thickness at incident electron energies of (a) 100 and (b) 300 keV. The structural information in the image is contributed through the interference between unscattered electrons (I_{noscat} , Eq. 108) and single elastic scattered electrons (I_{1el} , Eq. 109). The intensities for EPON are shown in Fig. 10.

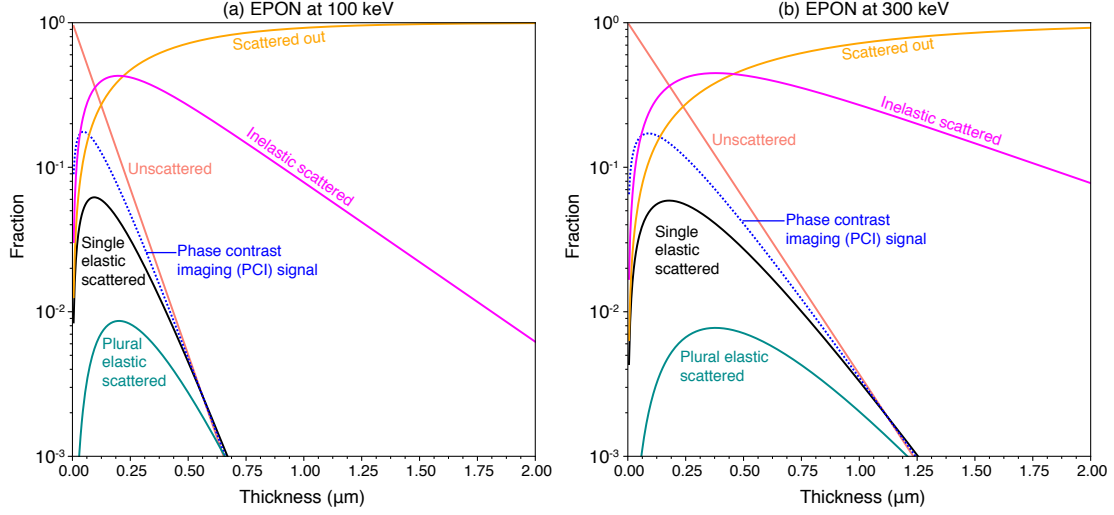


Figure 10: Normalized intensity profiles for phase contrast electron imaging in EPON as a function of thickness at incident electron energies of (a) 100 and (b) 300 keV. The intensities for amorphous ice are shown in Fig. 9.

6.4 Electron image contrast

The expressions of Eqs. 108–113 were for a uniform material. We now consider our model specimen as shown in Fig. 1, so that we can derive electron microscopy equivalents to the x-ray microscopy expressions of Eqs. 19, 20, 33, and 34. When the pixel of interest contains the background material, we obtain signal category intensities of

$$I_{\text{noscat},b} = I_0 e^{-(K_{\text{inel},b} + K_{\text{el},b})t} \quad (114)$$

$$\begin{aligned} I_{1\text{el},b} &= I_0 K_{\text{el},\text{in},b} e^{-(K_{\text{inel},b} + K_{\text{el},b})t} \\ &= K_{\text{el},\text{in},b} t I_{\text{noscat},b} \end{aligned} \quad (115)$$

$$I_{\text{in},\text{noinel},b} = I_0 e^{-(K_{\text{inel},b} + K_{\text{out},b})t} \quad (116)$$

$$I_{\text{el},\text{plural},b} = I_{\text{in},\text{noinel},b} - I_{\text{noscat},b} - I_{1\text{el},b} \quad (117)$$

$$I_{\text{in},b} = I_0 e^{-K_{\text{out},b}t} \quad (118)$$

$$I_{\text{inel},b} = I_{\text{in},b} - I_{\text{in},\text{noinel},b} \quad (119)$$

while when it contains the feature material we obtain

$$I_{\text{noscat},f} = I_0 e^{-(K_{\text{inel},b} + K_{\text{el},b})t_b} e^{-(K_{\text{inel},f} + K_{\text{el},f})t_f} \quad (120)$$

$$I_{1\text{el},f} = (K_{\text{el},\text{in},b} t_b + K_{\text{el},\text{in},f} t_f) I_{\text{noscat},f} \quad (121)$$

$$I_{1\text{el}/f,f} = K_{\text{el},\text{in},f} t_f I_{\text{noscat},f} \quad (122)$$

$$I_{\text{in},\text{noinel},f} = I_0 e^{-(K_{\text{out},b} + K_{\text{inel},b})t_b} e^{-(K_{\text{out},f} + K_{\text{inel},f})t_f} \quad (123)$$

$$I_{\text{el},\text{plural},f} = I_{\text{in},\text{noinel},f} - I_{\text{noscat},f} - I_{1\text{el},f} \quad (124)$$

$$I_{\text{in},f} = I_0 e^{-K_{\text{out},b}t_b} e^{-K_{\text{out},f}t_f} \quad (125)$$

$$I_{\text{inel},f} = I_{\text{in},f} - I_{\text{in},\text{noinel},f} \quad (126)$$

As noted in Sec. 1.1, phase contrast dominates in transmission electron microscopy of biological specimens. Phase contrast is usually obtained by using various defocus settings to maximize contrast at different momenta transfer values s [28, 29], though there have been advances in other approaches such as the Zernike method [74]. An additional improvement in image contrast [30, 31] can be obtained by isolating the “zero loss” electrons using an image filter (essentially an image-preserving electron monochromator located after

the objective lens); this excludes from the imaging plane the inelastically scattered electrons which have a different kinetic energy or de Broglie wavelength, so that they would otherwise contribute out-of-focus information to the usual image plane. We therefore need to account for phase contrast and zero-loss imaging using the intensity categories of Eqs. 114–126.

In electron microscopy, scattered electrons receive a phase shift of $\pi/2$ relative to the incident beam [68]; to maximize the image intensity difference caused by the presence or absence of these scattered electrons, their phase should be shifted by an additional $\pm\pi/2$ before being recombined with the incident beam at the location of the image pixel. As a result, the image intensity I_f resulting from a feature being present in the specimen is given by the interference between the unmodified incident wavefield $\Psi_{\text{noscat},f}$ and the $\pi/2$ -phase-shifted wavefield from the specimen feature $\Psi_{1\text{el},f}$, leading to an image intensity of

$$\begin{aligned} I_f &= |\Psi_{\text{noscat},f} + \Psi_{1\text{el},f}|^2 \\ &= I_{\text{noscat},f} + I_{1\text{el},f} + 2\sqrt{I_{\text{noscat},f}I_{1\text{el},f}}. \end{aligned} \quad (127)$$

If instead there is no feature present, then the background-material-containing pixel has no contrast variation within itself or relative to the surrounding material (Fig. 1), so its wavefield $\Psi_{1\text{el},b}$ will undergo no additional phase shift due to defocus, Zernike, or other phase contrast imaging methods in electron microscopy [28, 75]. As a result, the $\pi/2$ phase shift intrinsic to electron scattering will be unmodified, so that the intensity recorded in the background-material image pixel will be

$$\begin{aligned} I_b &= |\Psi_{\text{noscat},b} + |\Psi_{1\text{el},b}|e^{i\pi/2}|^2 \\ &= I_{\text{noscat},b} + I_{1\text{el},b}. \end{aligned} \quad (128)$$

We can therefore write the contrast parameter Θ of Eq. 7 as

$$\Theta_{\text{e,unfiltered}} = \frac{|I_{\text{noscat},f} - I_{\text{noscat},b} + I_{1\text{el},f} - I_{1\text{el},b}| + 2\sqrt{I_{\text{noscat},f}I_{1\text{el},f}}}{\sqrt{I_{\text{in},f} + I_{\text{in},b}}}. \quad (129)$$

when a zero-loss energy filter is absent, and

$$\Theta_{\text{e,filtered}} = \frac{|I_{\text{noscat},f} - I_{\text{noscat},b} + I_{1\text{el},f} - I_{1\text{el},b}| + 2\sqrt{I_{\text{noscat},f}I_{1\text{el},f}}}{\sqrt{I_{\text{in,noinel},f} + I_{\text{in,noinel},b}}}. \quad (130)$$

when a zero-loss energy filter is used. Note that the intensity $I_{\text{in,noinel}}$ contributes to the background when zero-loss filtering is not used, because these electrons will not be brought into a sharp focus on the pixel in the imaging plane due to their different de Broglie wavelength as noted above. Instead, they will be distributed in a more diffuse way on the detector plane, so that they effectively make equal contributions to the intensities of both feature and background pixels.

6.5 Electron imaging absorbed dose

Once we have the required per-pixel illumination of $\bar{n} = SNR^2/\Theta^2$ of Eq. 8 as calculated using either Eq. 129 or Eq. 130, we can calculate the radiation dose imparted to the specimen based on the fraction of inelastic scattering events and the mean energy $\langle\Delta E\rangle$ deposited per inelastic scatter (Eq. 103). The absorbed dose D_e , or energy deposited per mass in the pixel of area $\Delta^2 = t_f^2$, involves the fraction of interactions per length $K_{\text{inel},f}$ in the feature of thickness t_f (Eq. 42), leading to

$$D_e = \frac{SNR^2}{\Theta^2} \frac{\langle\Delta E\rangle K_{\text{inel},f}}{t_f^2 \rho_f}. \quad (131)$$

Note that because the rejection of any large-angle-scattered electrons by the objective aperture happens well downstream of the specimen plane, we do not include a term $[1 - I_{\text{out}}(t_{b,o})]$ which would otherwise indicate a reduction in the beam intensity due to any overlying background material. Finally, we can use Eqs. 42 and 131 to estimate a dose corresponding to a given electron fluence; for protein in amorphous ice, we find that a fluence of $1 \text{ e}^-/\text{nm}^2$ corresponds to a dose of 3.2×10^4 Gray at 100 kV, and 1.8×10^4 Gray at 300 kV.

7 Implications for various imaging scenarios

We have used a unified approach to estimate the required exposure and radiation dose in x-ray and electron microscopy. In this section, we make use of this approach to consider both the comparison of x-ray and electron microscopy, and to make several observations on the characteristics of x-ray microscopy and imaging. For these numerical calculations, we will use the complete expression for x-ray microscopy of Eq. 88, and the expressions for electron microscopy given in Eqs. 130 and 129 for the case of with and without zero-loss filtering, respectively.

7.1 Comparison with experimental results

Before making these comparisons, we first wish to check our calculations against some published experimental observations.

While many electron microscopy and tomography papers quote the electron fluence in e^-/nm^2 , relatively few provide precise quantitation of both the achieved spatial resolution and the overall specimen thickness. In addition, while in electron tomography one should have nearly the same dose as a 2D image due to the dose fractionation theorem noted above [47], errors in the alignment of projection images onto a common axis of rotation can degrade image quality [49] and thus bias reported results towards a higher electron fluence than might otherwise have been necessary. While there have been advances in methods for tomogram alignment [76], details such as the results of alignment convergence tests are almost never reported. In addition, single-particle imaging results are not directly relevant to our comparison as they involve combining the signals from independent images of a large number of identical particles [14, 15, 77]. For these reasons, the best comparison is to consider 2D imaging of thicker specimens. In 120 kV zero-loss images of tobacco mosaic virus in $t_b = 100$ nm thick amorphous ice, fluence/resolution combinations $10 e^-/\text{nm}^2$ at 4 nm, $300 e^-/\text{nm}^2$ at 0.7 nm, and $1200 e^-/\text{nm}^2$ at 0.4 nm resolution have been reported [78]. Our calculations provide estimates of $\bar{n} = 14$ at $t_f = 4$ nm, $\bar{n} = 470$ at $t_f = 0.7$ nm, and $\bar{n} = 1430$ at 0.4 nm resolution, in all cases within 20–60% of the experimental observations. We consider this to be a reasonable agreement.

In x-ray microscopy, there are again only a limited number of examples of 2D imaging of frozen hydrated specimens where the detection efficiency is well known. One such example involves 5.2 keV x-ray ptychography as a method for phase contrast imaging of a frozen hydrated cell with an overall ice thickness of $t_b = 3 \mu\text{m}$, where a fluence of 9.2×10^3 photons/ nm^2 was used to achieve sub-20 nm resolution [79]. Our calculation provides an estimate of $\bar{n} = 11.3 \times 10^3$ photons/ nm^2 at $t_f = 20$ nm, again showing quite reasonable agreement.

7.2 A comparison of x-ray and electron microscopy

In Section 1.1, we noted that previous comparisons of x-ray and electron microscopy arrived at seemingly contradictory statements about their relative merits. By using a consistent methodology, we are able to address this question, building upon previous work [26] by including inelastic and plural elastic scattering effects in x-ray microscopy as well as in electron microscopy.

Because radiation dose scales strongly with spatial resolution, we consider the case of a fixed spatial resolution of 10 nm which is routine in electron microscopy and is within a factor of 2 of what is now being demonstrated x-ray microscopy of frozen hydrated biological specimens [79]. (Even at slightly coarser resolution, x-ray microscopy can be used to study structural changes in mitochondria associated with virus infections [80], while only slight improvements in resolution are required for electron tomography studies of actin networks [81]). Therefore we show in Fig. 11 the estimated radiation dose for imaging 10 nm protein features in amorphous ice thicknesses ranging from 50 nm (typical of nicely-blotted plunge-frozen specimens of macromolecules or virions), to $\sim 0.5 \mu\text{m}$ (typical of whole archaebacteria [34] as well as peripheral regions of adherent eukaryotic cells [82]), to thicknesses of $10 \mu\text{m}$ (representative of the yeast *S. cerevisiae* [83]), and beyond. Examination of Fig. 11 allows us to state the following:

- Electron microscopy offers dramatically lower radiation dose for high resolution imaging when the specimen thickness is much less than about $0.3 \mu\text{m}$, with extendability to slightly more than $1 \mu\text{m}$ for zero-loss imaging at 300 kV.

- X-ray microscopy offers lower dose at thicknesses greater than about 1 μm . At the soft x-ray energy of 0.5 keV corresponding to the “water window” [84] between the carbon K absorption edge at 0.29 keV and the oxygen K edge at 0.54 eV, Zernike phase contrast provides some improvement over absorption contrast [52, 24, 25, 8] in terms of minimum dose imaging. At x-ray energies above the oxygen K edge, absorption contrast becomes unfavorable; however, at energies greater than about 2 keV, phase contrast becomes quite favorable so that one can image features in amorphous ice layers as thick as several tens of micrometers [23, 24, 25, 27].

In other words, Fig. 11 makes it clear that the seemingly-contradictory prior conclusions outlined in Sec. 1.1 are both correct.

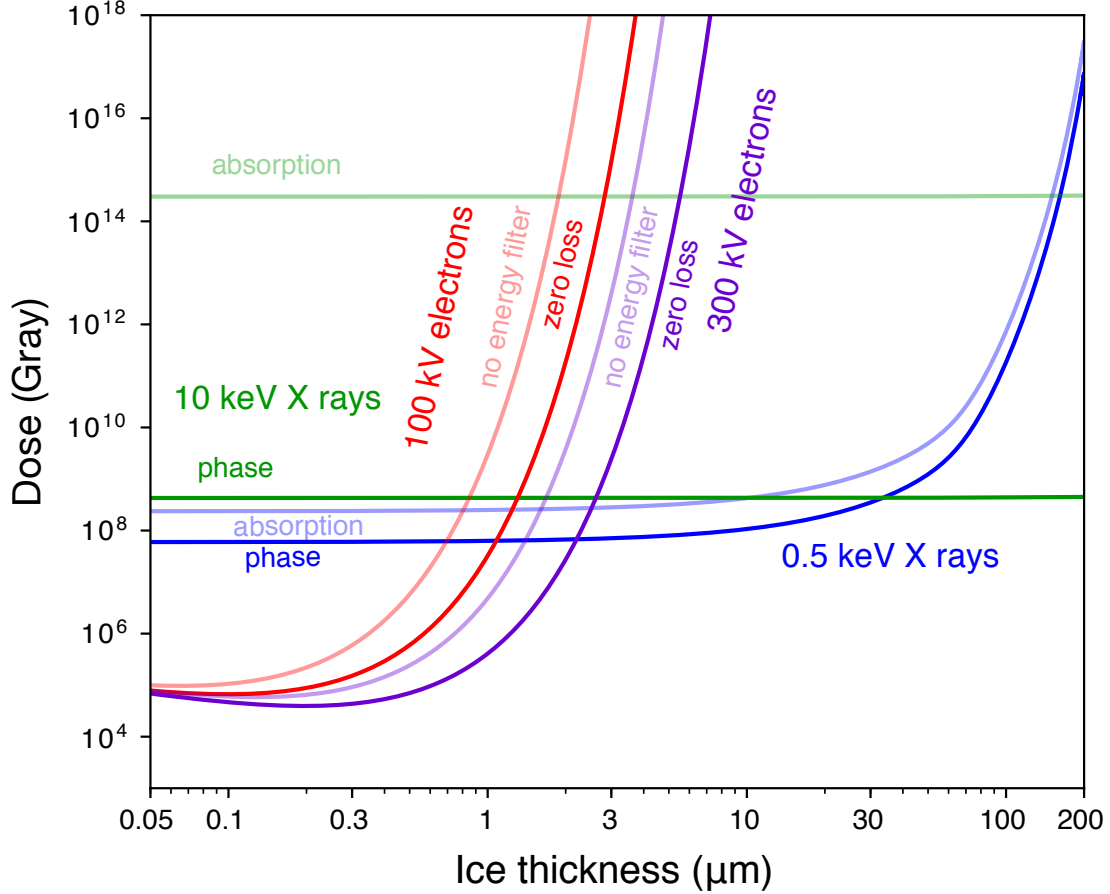


Figure 11: Estimated radiation dose associated with 10 nm resolution imaging of protein features in amorphous ice. This shows the case for soft x-ray microscopy at 0.5 keV and hard x-ray microscopy at 10 keV, both for absorption and Zernike phase contrast. In the case of electron microscopy, accelerating voltages of 100 and 300 kV are shown for phase contrast imaging with and without the use of a zero-loss energy filter. In all cases, the imaging system is assumed to have 100% efficiency.

In order to better understand the optimal photon energy to be used for transmission imaging in x-ray microscopy, in Fig. 12 we show the dose required for $SNR=5$ imaging of 10 nm protein features as a function of both x-ray energy and overall amorphous ice thickness. Once again, this figure shows the advantages of the “water window” spectral region [84], as well as the utility of phase contrast imaging at energies above about 2 keV.

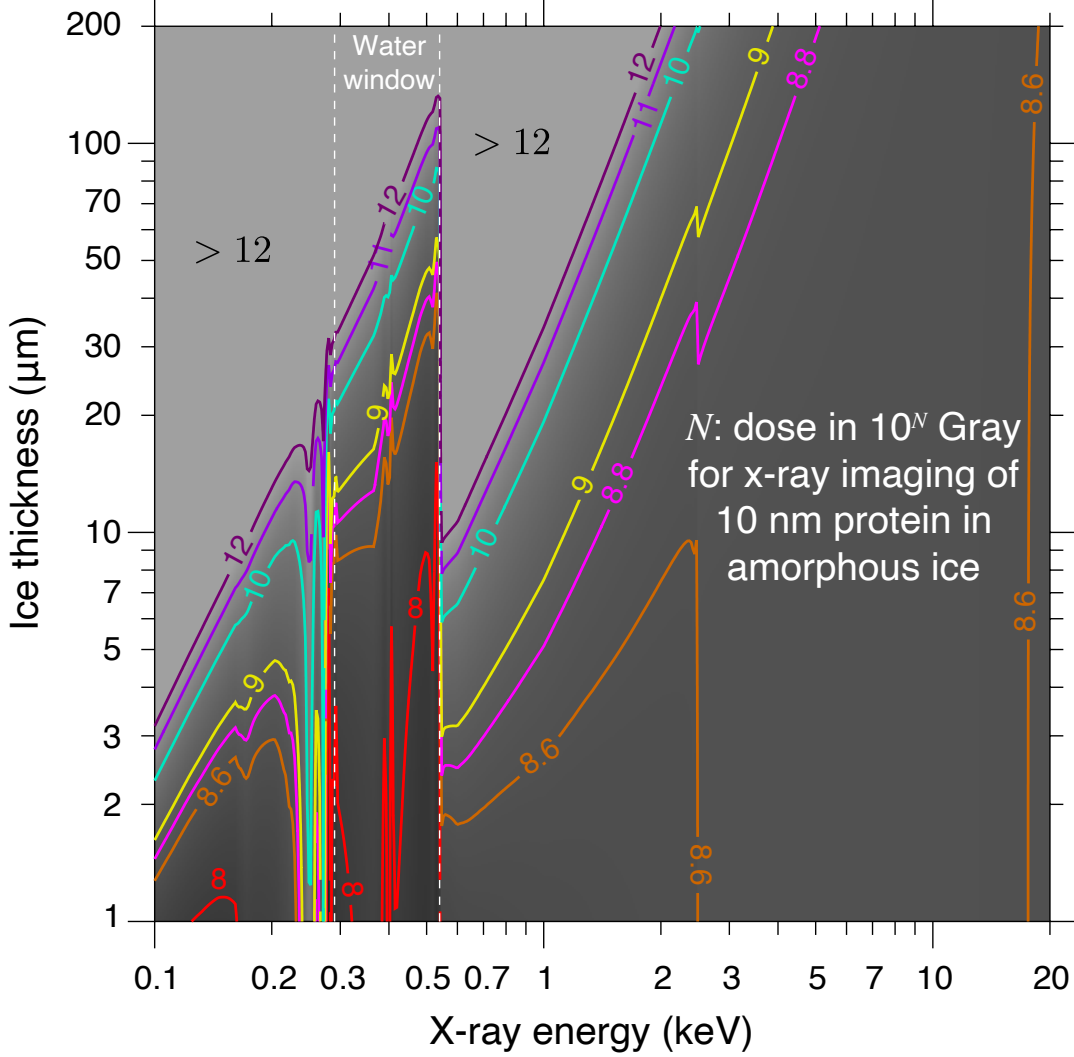


Figure 12: Combined contour and brightness map of the required x-ray radiation dose in Gray for imaging 10 nm features in amorphous ice as a function of both x-ray photon energy and overall ice thickness. This figure shows the lower of absorption or phase contrast imaging at each point; in nearly all cases phase contrast provides the lowest dose. The grayscale image shows $\log_{10}(\text{Gray})$, with the overlaying contour line labeled 6 representing a dose of 10^6 Gray and so on. The soft x-ray “water window” energy range [84] between the carbon *K* edge at 0.29 keV and the oxygen *K* edge at 0.54 eV provides minimum dose imaging for specimens in ice layers up to about 10–20 μm thick, while phase contrast requires a slightly higher dose at multi-keV energies while accommodating thicker specimens overall. Note that the presence of sulfur in our model protein leads to the contour feature at the *S K* edge at 2.47 keV.

7.3 Dose versus resolution in x-ray microscopy

As discussed in Sec. 3.1 and shown in the approximate results of Eqs. 94 and 95, for isotropic features the required radiation dose in x-ray microscopy increase as the fourth power of improvements in spatial resolution. Therefore in Fig. 13 we show the required dose associated with $SNR=5$ x-ray imaging of protein features in 10 μm thick amorphous ice as the size and thickness t_f of the features is changed, as calculated using the complete expression of Eq. 88. As one decreases t_f from 1 μm towards 1 nm, the calculated dose changes by about 12 orders of magnitude so we also show on this figure the threshold doses associated with a variety of radiation-induced phenomena:

- The human LD₅₀ dose of about 4.5 Gray, which is the radiation dose that leads to to 50% fatalities in human populations [85].
- The incapacitation dose for rats and pigs, which is the dose at which these animals show an immediate cessation of normal function when the dose is administered over a time of minutes or less. Miniature pigs used in animal agriculture show immediate incapacitation upon exposure to gamma and neutron radiation doses of 130 Gray [86], while male albino rats show immediate incapacitation at radiation doses of 153 Gray [87].
- The LD₁₀ dose for the radiation-resistant bacterium *Deinococcus radiodurans*. This dose of $1.0\text{--}2.5 \times 10^3$ Gray kills all but 10% of these bacteria in sewage sludge or animal feed [88].
- The dose associated with immediate inactivation of muscle function. At an absorbed soft x-ray dose of about 2×10^4 Gray, myofibrils will no longer contract in response to the addition of adenosine triphosphate or ATP [89].
- The dose associated with immediate structural changes in living cells. Chinese hamster ovarian cells show no immediate effect at soft x-ray doses of about 6×10^2 Gray, but they show immediate and dramatic structural changes at a dose of 1.2×10^5 Gray [90].
- The dose associated with changes in the carbon x-ray absorption near-edge structure (XANES) of polymers. One can observe an $\exp[-1]$ decrease in the strength of the C=C absorption resonance in room temperature polymethyl methacrylate (PMMA) at a dose of about 1.2×10^7 Gray [91], or in the C=O absorption resonance in PMMA at a temperature of 113 K at a dose of 1.3×10^7 Gray [92].
- The so-called Henderson dose limit for fading of x-ray diffraction spots in cryo-cooled crystals of about 2×10^7 Gray [93]. It should be noted that a more recent evaluation has suggested that a dose of 3×10^7 Gray represents a tolerable limit [94]; in fact, there is some dependence on the length scale of bond-to-bond correlations (as measured from the diffraction angle of various Bragg peaks) as shown in Fig. 3 of [44].
- The dose associated with mass loss in PMMA at a cryogenic temperature of 113 K. Soft x-ray measurements have shown [92] an $\exp[-1]$ decrease in oxygen mass in PMMA films exposed to a dose of 6.0×10^8 Gray at this temperature. It should be noted that PMMA is one of the more radiation-sensitive polymers, which is why it is used as a photoresist in electron beam lithography; polymers with aromatic rings as part of the monomer units are much more robust against mass loss.
- The dose associated with “bubbling” of amorphous ice in electron microscopy [51], which involves the dissociation of H₂O to form hydrogen bubbles [95]. Though the dose varies with specimen conditions, an electron fluence of $5000 \text{ e}^-/\text{nm}^2$ at 100 kV (corresponding to a dose of about 1.6×10^{11} Gray) is representative.

Of these effects, all but the last two are measures either of biological function, or specific atomic bonding or atom-to-atom correlation distances. For microscopy at a resolution of a few nanometers, these effects do not affect the image (unless one is utilizing XANES resonances for image contrast [96]); however, the last two measures (mass loss and amorphous ice “bubbling”) represent harder limits. For this reason, earlier studies on dose limits to resolution in x-ray microscopy based on diffraction spot fading [44] may be overly pessimistic.

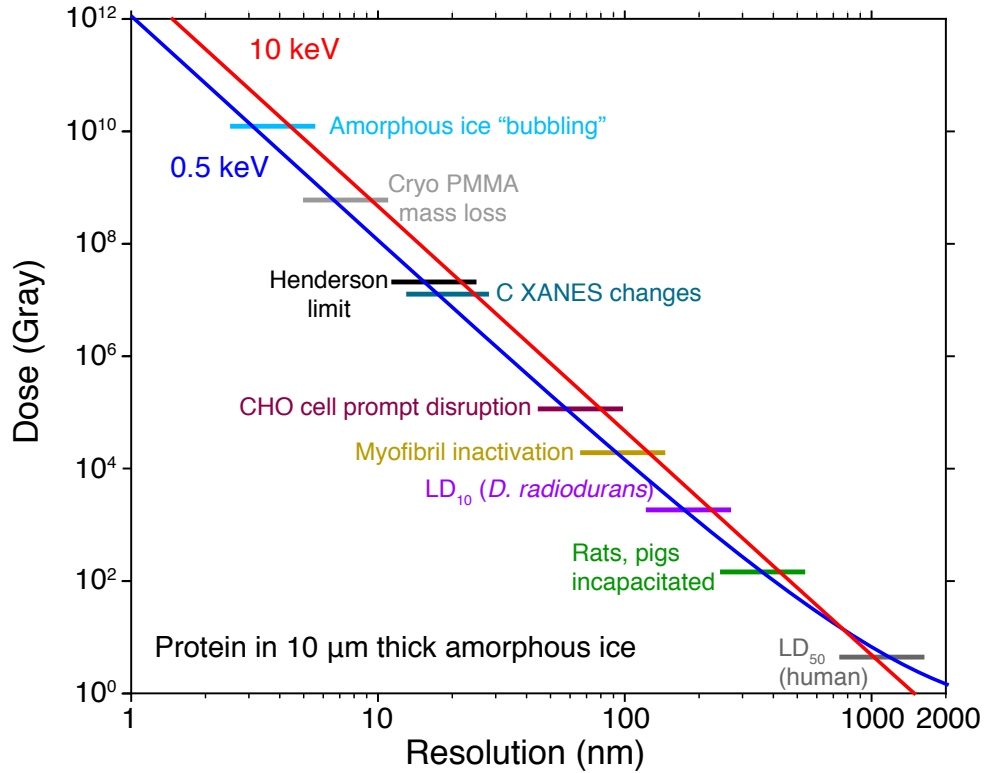


Figure 13: Required radiation dose as a function of resolution. In this case of imaging protein in 10 μm of amorphous ice, the dose for $SNR=5$ imaging was calculated as t_F was varied, for both soft x-rays in the water window (0.5 keV) or for hard X rays (10 keV), for the better of absorption or Zernike phase contrast at each thickness. The trend of required dose increasing as the fourth power of improvements in spatial resolution (decreases in t_f) as expected from Eqs. 94 and 95 is clearly seen. Also shown are the radiation doses associated with various detrimental effects in biological specimens, as discussed in Sec. 7.3.

7.4 Ultimate thickness limits in x-ray microscopy

In Sec. 7.2, we compared electron and x-ray microscopy for 10 nm resolution imaging in amorphous ice thicknesses up to 200 μm and with x-ray energies as high as 20 keV, as shown in Figs. 11 and 12. We also saw in Fig. 13 that the required x-ray dose increases as the fourth power of improvements in spatial resolution (corresponding to decreases in t_f). We now consider a somewhat different imaging regime: mesoscale resolution imaging with $t_f = 100$ nm for very thick specimens, such as might be desired for x-ray imaging of whole mouse brains in neuroanatomical studies [97, 98]. While these studies are presently done with metal-stained, plastic-embedded specimens, we have chosen to do a calculation for the case of protein in amorphous ice for three reasons: 1) more direct comparison with the previous figures; 2) because the general characteristics of inelastic and plural elastic scattering shown in Figs. 2 and 3 are not qualitatively different between amorphous ice and EPON; and 3) because it could be useful to consider native image contrast should a means be found to minimize ice crystal formation at 100 nm resolution in whole-organ-size specimens. We therefore show in Fig. 14 the results of a calculation for amorphous ice thicknesses of 1 to 100 μm , and for x-ray energies ranging from 5 to 50 keV. As this figure shows, once one has reached an x-ray energy sufficiently high enough to obtain good penetration through the specimen, the required radiation dose shows very little variation with further changes in photon energy. This is consistent with what one would expect from the thin-specimen dose approximation of Eq. 96 even though the background thickness is considerably higher here. For real specimens of this thickness, there will be significant problems in interpreting 2D images because of the overlap of features at many depth planes in a projection, but this is what tomography

untangles and again we would expect dose fractionation [47] to mean that this untangling does not come at a severe penalty in additional radiation dose.

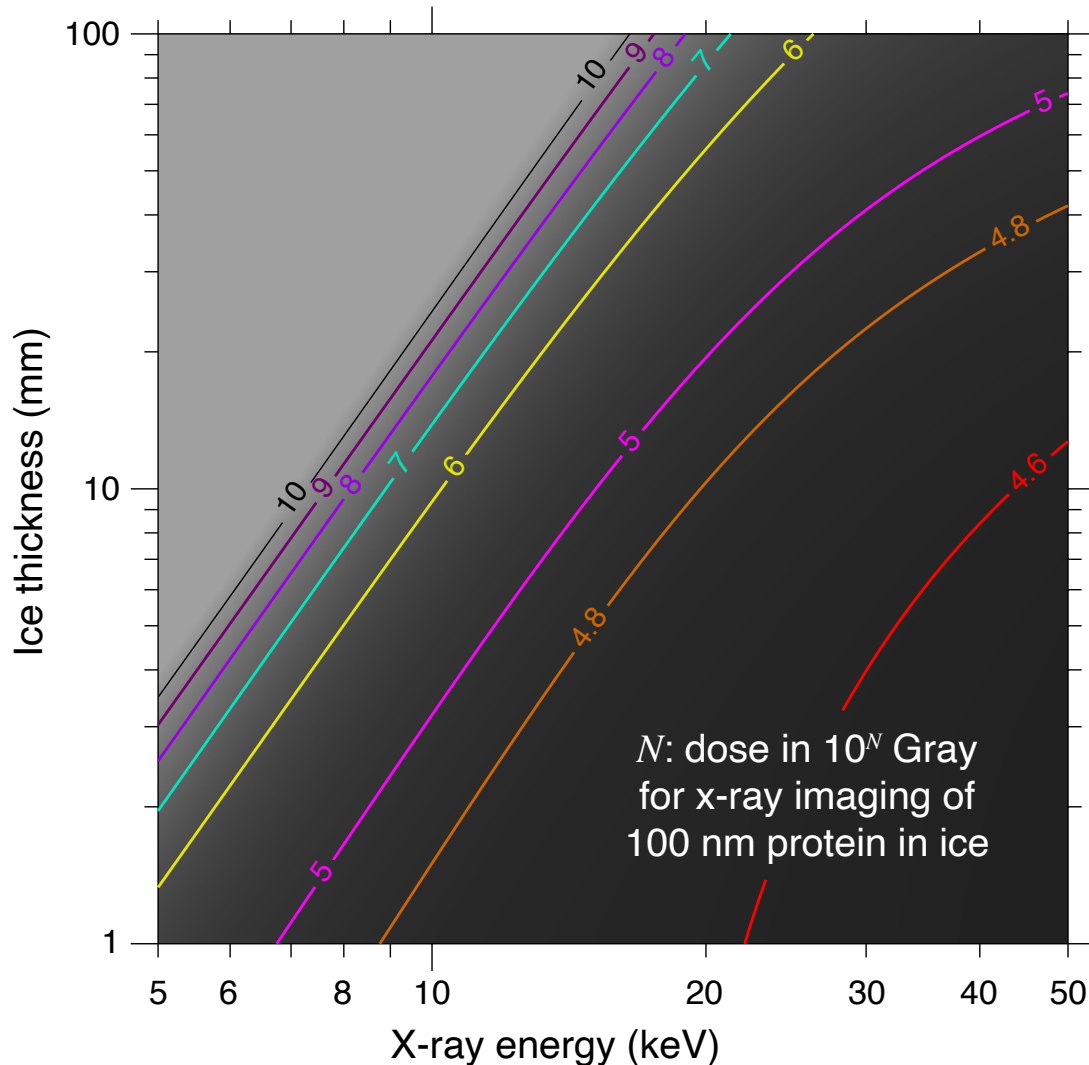


Figure 14: Combined contour and brightness map of the required x-ray radiation dose in Gray for imaging 100 nm features in amorphous ice as a function of both x-ray photon energy and overall ice thickness. This figure shows the lower of absorption or phase contrast imaging at each point; in nearly all cases phase contrast provides the lowest dose. The grayscale image shows $\log_{10}(\text{Gray})$, with the overlaying contour line labeled 6 representing a dose of 10^6 Gray and so on. Of course it would be very challenging to obtain amorphous ice over these organ-scale thicknesses, but on the other hand ice crystal artifacts that obscure features in few-nanometer-resolution cryo electron microscopy studies might be unnoticeable in 100 nm resolution imaging.

8 Conclusion

We have described a consistent approach to estimating the required per-pixel quantum exposure \bar{n} and associated radiation dose D for both x-ray and electron microscopy of thick specimens, and have applied these calculations to the example of imaging frozen hydrated as well as plastic embedded biological specimens. We have done so by building upon previous work in x-ray [21, 22, 24, 25, 26, 8, 27] and electron [32, 33, 34]

microscopy, but with an accounting of inelastic and plural elastic scattering, zero-loss energy filtering in electron microscopy, and phase contrast in both x-ray and electron microscopy. From a radiation dose point of view, these calculations reinforce the idea that electron microscopy offers advantages for specimens thinner than about 1 micrometer (unless one wishes to obtain chemical contrast using near-absorption-edge spectra [99, 100], or if one seeks maximum sensitivity in trace element mapping [38, 101, 102]), while x-ray microscopy becomes the method of choice for thicker specimens.

Acknowledgement

We gratefully acknowledge support from the National Institutes of Health for support under grant U01 MH109100, and the Advanced Photon Source, a US Department of Energy (DoE) Office of Science User Facility operated under contract DE-AC02-06CH11357. We also thank Dr. Qiaoling Jin for preparation of an EPON sample and Dr. Kai He for assistance with EELS measurements on that sample at Northwestern University, and Dr. Richard Leapman of the National Institutes of Health for the amorphous ice EELS data shown in Fig. 8.

References

References

- [1] M. G. Gustafsson, Surpassing the lateral resolution limit by a factor of two using structured illumination microscopy, *Journal of Microscopy* 198 (2) (2000) 82–87.
- [2] M. Burton, General discussion, *Discussions of the Faraday Society* 12 (1952) 317–318.
- [3] A. Chapiro, *Radiation Chemistry of Polymeric Systems*, Interscience Publishers, 1962.
- [4] B. W. Low, C. C. Chen, J. E. Berger, L. Singman, J. F. Pletcher, Studies of insulin crystals at low temperatures: effects on mosaic character and radiation sensitivity, *Proceedings of the National Academy of Sciences* 56 (6) (1966) 1746–1750.
- [5] D. J. Haas, M. G. Rossmann, Crystallographic studies on lactate dehydrogenase at -75°C , *Acta Crystallographica B* 26 (7) (1970) 998–1004.
- [6] K. Taylor, R. Glaeser, Electron diffraction of frozen, hydrated protein crystals, *Science* 106 (1974) 1036–1037.
- [7] J. Dubochet, M. Adrian, J. Chang, J.-C. Homo, J. Lepault, A. McDowell, P. Schultz, Cryo-electron microscopy of vitrified specimens, *Quarterly Reviews of Biophysics* 21 (1988) 129–228.
- [8] G. Schneider, Cryo x-ray microscopy with high spatial resolution in amplitude and phase contrast, *Ultramicroscopy* 75 (1998) 85–104.
- [9] J. Maser, A. Osanna, Y. Wang, C. Jacobsen, J. Kirz, S. Spector, B. Winn, D. Tennant, Soft x-ray microscopy with a cryo STXM: I. Instrumentation, imaging, and spectroscopy, *Journal of Microscopy* 197 (1) (2000) 68–79.
- [10] M. Tinone, K. Tanaka, N. Ueno, Photodecomposition of poly(methylmethacrylate) thin films by monochromatic soft x-ray radiation, *Journal of Vacuum Science and Technology A* 13 (4) (1995) 1885–1892.
- [11] J. R. Breedlove Jr., G. Trammel, Molecular microscopy: fundamental limitations, *Science* 170 (1970) 1310–1313.
- [12] R. Henderson, The potential and limitations of neutrons, electrons and X-rays for atomic resolution microscopy of unstained biological molecules, *Quarterly Reviews of Biophysics* 28 (2) (1995) 171–193.

- [13] R. M. Glaeser, Limitations to significant information in biological electron microscopy as a result of radiation damage, *Journal of Ultrastructure Research* 36 (3-4) (1971) 466–482.
- [14] J. Frank, W. Goldfarb, D. Eisenberg, T. S. Baker, Reconstruction of glutamine synthetase using computer averaging, *Ultramicroscopy* 3 (3) (1978) 283–290.
- [15] J. Frank, A. Verschoor, M. Boublik, Computer averaging of electron micrographs of 40S ribosomal subunits, *Science* 214 (4527) (1981) 1353–1355.
- [16] W. Kühlbrandt, The resolution revolution, *Science* 343 (6178) (2014) 1443–1444.
- [17] J. C. Solem, G. C. Baldwin, Microholography of living organisms, *Science* 218 (1982) 229–235.
- [18] R. Neutze, R. Wouts, D. van der Spoel, E. Weckert, J. Hajdu, Potential for biomolecular imaging with femtosecond x-ray pulses, *Nature* 406 (2000) 752–757.
- [19] W. E. King, G. H. Campbell, A. Frank, B. Reed, J. F. Schmerge, B. J. Siwick, B. C. Stuart, P. M. Weber, Ultrafast electron microscopy in materials science, biology, and chemistry, *Journal of Applied Physics* 97 (11) (2005) 111101.
- [20] R. M. Glaeser, Retrospective: radiation damage and its associated “information limitations”, *Journal of Structural Biology* 163 (3) (2008) 271–276.
- [21] D. Sayre, J. Kirz, R. Feder, D. M. Kim, E. Spiller, Transmission microscopy of unmodified biological materials. comparative radiation dosages with electrons and ultrasoft x-ray photons, *Ultramicroscopy* 2 (1977) 337–349.
- [22] D. Sayre, J. Kirz, R. Feder, D. M. Kim, E. Spiller, Potential operating region for ultrasoft x-ray microscopy of biological materials, *Science* 196 (4296) (1977) 1339–1340.
- [23] G. Schmahl, D. Rudolph, Proposal for a phase contrast x-ray microscope, in: P. C. Cheng, G. J. Jan (Eds.), *X-ray Microscopy: Instrumentation and Biological Applications*, Springer-Verlag, Berlin, 1987, pp. 231–238.
- [24] P. Götz, Calculations on radiation dosages of biological materials in phase contrast and amplitude contrast x-ray microscopy, in: Michette et al. [103], pp. 313–315.
- [25] C. Jacobsen, Making soft x-ray microscopy harder: considerations for sub-0.1 μm resolution imaging at $\sim 4 \text{ \AA}$ wavelengths, in: Michette et al. [103], pp. 274–277.
- [26] C. Jacobsen, R. Medenwaldt, S. Williams, A perspective on biological x-ray and electron microscopy, in: J. Thieme, G. Schmahl, E. Umbach, D. Rudolph (Eds.), *X-ray Microscopy and Spectromicroscopy*, Springer-Verlag, Berlin, 1998, pp. II–93–102.
- [27] Z. Wang, K. Gao, J. Chen, Y. Hong, X. Ge, D. Wang, Z. Pan, P. Zhu, W. Yun, C. Jacobsen, Z. Wu, Advantages of intermediate x-ray energies in zernike phase contrast x-ray microscopy, *Biotechnology Advances* 31 (3) (2013) 387–392.
- [28] D. J. Johnson, Amplitude and phase contrast in electron-microscope images of molecular structures, *Journal of the Royal Microscopical Society* 88 (1) (1968) 39–47.
- [29] P. N. T. Unwin, Phase contrast electron microscopy of biological materials, *Journal of Microscopy* 98 (3) (1973) 299–312.
- [30] R. Bauer, Electron spectroscopic imaging: An advanced technique for imaging and analysis in transmission electron microscopy, *Methods in Microbiology* 20 (6) (1988) 113–146.
- [31] R. R. Schröder, W. Hofmann, J.-F. Ménéret, Zero-loss energy filtering as improved imaging mode in cryoelectronmicroscopy of frozen-hydrated specimens, *Journal of Structural Biology* 105 (1990) 28–34.

- [32] R. R. Schröder, Zero-loss energy-filtered imaging of frozen-hydrated proteins: model calculations and implications for future developments, *Journal of Microscopy* 166 (1992) 389–400.
- [33] J. P. Langmore, M. F. Smith, Quantitative energy-filtered electron microscopy of biological molecules in ice, *Ultramicroscopy* 46 (1992) 349–373.
- [34] R. Grimm, H. Singh, R. Rachel, D. Typke, W. Zillig, W. Baumeister, Electron tomography of ice-embedded prokaryotic cells, *Biophysical Journal* 74 (2) (1998) 1031–1042.
- [35] W. Hoppe, Das Endlichkeitspostulat und das Interpolationstheorem der dreidimensionalen elektronenmikroskopischen Analyse aperiodischer Strukturen, *Optik* 29 (1969) 617–621.
- [36] R. A. Crowther, D. J. DeRosier, A. Klug, The reconstruction of a three-dimensional structure from projections and its application to electron microscopy, *Proceedings of the Royal Society of London A* 317 (1530) (1970) 319–340.
- [37] X. Huang, H. Miao, J. Steinbrener, J. Nelson, D. Shapiro, A. Stewart, J. Turner, C. Jacobsen, Signal-to-noise and radiation exposure considerations in conventional and diffraction x-ray microscopy, *Optics Express* 17 (16) (2009) 13541–13553. doi:10.1364/OE.17.013541.
- [38] J. Kirz, D. Sayre, J. Dilger, Comparative analysis of x-ray emission microscopies for biological specimens, pp. 291–305.
- [39] Y. Sun, S.-C. Gleber, C. Jacobsen, J. Kirz, S. Vogt, Optimizing detector geometry for trace element mapping by x-ray fluorescence, *Ultramicroscopy* 152 (C) (2015) 44–56.
- [40] J. C. Solem, Imaging biological specimens with high-intensity soft x rays, *Journal of the Optical Society of America B* 3 (1986) 1551–1565.
- [41] R. A. London, M. D. Rosen, J. E. Trebes, Wavelength choice for soft x-ray laser holography of biological samples, *Applied Optics* 28 (16) (1989) 3397–3404.
- [42] Q. Shen, I. Bazarov, P. Thibault, Diffractive imaging of nonperiodic materials with future coherent x-ray sources, *Journal of Synchrotron Radiation* 11 (2004) 432–438.
- [43] D. Sarodub, P. Rez, G. Hembree, M. Howells, D. Shapiro, H. Chapman, P. Fromme, K. Schmidt, U. Weierstall, R. B. Doak, J. C. H. Spence, Dose, exposure time and resolution in serial x-ray crystallography, *Journal of Synchrotron Radiation* 15 (2008) 62–73.
- [44] M. R. Howells, T. Beetz, H. N. Chapman, C. Cui, J. M. Holton, C. J. Jacobsen, J. Kirz, E. Lima, S. Marchesini, H. Miao, D. Sayre, D. A. Shapiro, J. C. H. Spence, D. Starodub, An assessment of the resolution limitation due to radiation-damage in x-ray diffraction microscopy, *Journal of Electron Spectroscopy and Related Phenomena* 170 (2009) 4–12.
- [45] A. Schropp, C. G. Schroer, Dose requirements for resolving a given feature in an object by coherent x-ray diffraction imaging, *New Journal of Physics* 12 (3) (2010) 035016.
- [46] L. Grodzins, Optimum energies for x-ray transmission tomography of small samples, *Nuclear Instruments and Methods in Physics Research* 206 (3) (1983) 541–545.
- [47] R. Hegerl, W. Hoppe, Influence of electron noise on three-dimensional image reconstruction, *Zeitschrift für Naturforschung* 31 a (1976) 1717–1721.
- [48] W. Hoppe, R. Hegerl, Some remarks concerning the influence of electron noise on 3D reconstruction, *Ultramicroscopy* 6 (1981) 205–206.
- [49] B. F. McEwen, K. H. Downing, R. M. Glaeser, The relevance of dose-fractionation in tomography of radiation-sensitive specimens, *Ultramicroscopy* 60 (1995) 357–373.
- [50] A. Rose, Unified approach to performance of photographic film, television pickup tubes, and human eye, *Journal of the Society of Motion Picture Engineers* 47 (1946) 273–294.

- [51] J. Dubochet, J. Lepault, R. Freeman, J. A. Berriman, J.-C. Homo, Electron-microscopy of frozen water and aqueous-solutions, *Journal of Microscopy* 128 (3) (1982) 219–237.
- [52] D. Rudolph, G. Schmahl, B. Niemann, Amplitude and phase contrast in x-ray microscopy, in: P. J. Duke, A. G. Michette (Eds.), *Modern Microscopies*, Plenum, New York, 1990, pp. 59–67.
- [53] A. Einstein, Lassen sich Brechungsexponenten der korper für Röntgenstrahlen experimentell ermitteln?, *Verhandlungen der Deutschen Physikalischen Gesellschaft* 9 (12) (1918) 86–87.
- [54] A. H. Compton, The total reflexion of x-rays, *Philosophical Magazine* 45 (270) (1923) 1121–1131.
- [55] B. L. Henke, E. M. Gullikson, J. C. Davis, X-ray interactions: Photoabsorption, scattering, transmission, and reflection at $E=50\text{--}30,000$ eV, $Z=1\text{--}92$, *Atomic Data and Nuclear Data Tables* 54 (1993) 181–342.
- [56] W. T. Elam, B. D. Ravel, J. R. Sieber, A new atomic database for x-ray spectroscopic calculations, *Radiation Physics and Chemistry* 63 (2) (2002) 121–128.
- [57] T. Schoonjans, A. Brunetti, B. Golosio, M. S. del Rio, V. A. Solé, C. Ferrero, L. Vincze, The xraylib library for x-ray–matter interactions. Recent developments, *Spectrochimica Acta Part B* 66 (11–12) (2011) 776–784.
- [58] F. Zernike, Beugungstheorie des schneidenver-fahrens und seiner verbesserten form, der phasenkontrastmethode, *Physica* 1 (1934) 689–704.
- [59] F. Zernike, Phase contrast, a new method for microscopic observation of transparent objects. part i, *Physica* 9 (1942) 686–698.
- [60] F. Zernike, Phase-contrast, a new method for microscopic observation of transparent objects. part ii, *Physica* 9 (1942) 974–986.
- [61] S. W. Wilkins, Y. I. Nesterets, T. E. Gureyev, S. C. Mayo, A. Pogany, A. W. Stevenson, On the evolution and relative merits of hard x-ray phase-contrast imaging methods, *Philosophical Transactions of the Royal Society of London A* 372 (2010) (2014) 20130021–20130021.
- [62] J. H. Hubbell, W. J. Veigele, E. A. Briggs, Atomic form factors, incoherent scattering functions and photon scattering cross sections, *Journal of Physical and Chemical Reference Data* 4 (1975) 471–538.
- [63] J. H. Hubbell, H. A. Gimm, I. Øverbø, Pair, triplet, and total atomic cross sections (and mass attenuation coefficients) for 1 MeV–100 GeV photons in elements $Z = 1$ to 100, *Journal of Physical and Chemical Reference Data* 9 (4) (1980) 1023–126.
- [64] S. H. Dietze, O. G. Shpyrko, Coherent diffractive imaging: towards achieving atomic resolution, *Journal of Synchrotron Radiation* 22 (2015) 1498–1508.
- [65] E. Valentini, A. G. Kikhney, G. Previtali, C. M. Jeffries, D. I. Svergun, SASBDB, a repository for biological small-angle scattering data, *Nucleic Acids Research* 43 (D1) (2015) D357–D363.
- [66] H. Bethe, Theorie der Beugung von Elektronen an Kristallen, *Annalen der Physik* 392 (17) (1928) 55–129.
- [67] H. Wyrwich, F. Lenz, Berechnung der differentiellen Wirkungsquerschnitte für die Streuung mittelschneller Elektronen an Atomen aus Hartree-Funktionen, *Zeitschrift Fur Naturforschung A* 13 (7) (1958) 515–523.
- [68] L. Reimer, *Transmission electron microscopy: physics of image formation and microanalysis*, 3rd Edition, Springer-Verlag, Berlin, 1993, springer Series in Optical Sciences **36**.
- [69] D. B. Williams, C. B. Carter, *Transmission electron microscopy: a textbook for materials science*, Springer, Boston, MA, 1996.

- [70] D. Johnson, J. Spence, Determination of the single-scattering probability distribution from plural-scattering data, *Journal of Physics D* 7 (6) (1974) 771–780.
- [71] F. Wang, R. Egerton, M. Malac, Fourier-ratio deconvolution techniques for electron energy-loss spectroscopy (EELS), *Ultramicroscopy* 109 (10) (2009) 1245–1249.
- [72] M. Isaacson, D. Johnson, A. V. Crewe, Electron beam excitation and damage of biological molecules: its implications for specimen damage in electron microscopy, *Radiation Research* 55 (1973) 205–224.
- [73] M. Isaacson, Inelastic scattering and beam damage of biological molecules, in: B. M. Siegel, D. R. Beaman (Eds.), *Physical aspects of electron microscopy and microbeam analysis*, Wiley, New York, 1975, pp. 247–258.
- [74] R. M. Glaeser, Methods for imaging weak-phase objects in electron microscopy, *Review of Scientific Instruments* 84 (11) (2013) 111101.
- [75] D. J. Johnson, D. Crawford, Defocusing phase contrast effects in electron microscopy, *Journal of Microscopy* 98 (3) (1973) 313–324.
- [76] F. Amat, D. Castaño-Diez, A. Lawrence, F. Moussavi, H. Winkler, M. Horowitz, Alignment of cryo-electron tomography datasets, *Methods in Enzymology* 482 (2010) 343–367.
- [77] J. Frank, Single-particle imaging of macromolecules by cryo-electron microscopy, *Annual Review of Biophysics and Biomolecular Structure* 31 (2002) 303–319.
- [78] R. Grimm, A. J. Koster, U. Ziese, D. Typke, W. Baumeister, Zero-loss energy filtering under low-dose conditions using a post column energy filter, *Journal of Microscopy* 183 (1996) 60–68.
- [79] J. Deng, D. J. Vine, S. Chen, Q. Jin, Y. S. G. Nashed, T. Peterka, S. Vogt, C. Jacobsen, X-ray ptychographic and fluorescence microscopy of frozen-hydrated cells using continuous scanning, *Scientific Reports* 7 (1) (2017) 445.
- [80] A. J. Pérez-Berná, M. J. Rodríguez, F. J. Chichón, M. F. Friesland, A. Sorrentino, J. L. Carrascosa, E. Pereiro, P. Gastaminza, Structural Changes In Cells Imaged by Soft X-ray Cryo-Tomography During Hepatitis C Virus Infection, *ACS Nano* 10 (7) (2016) 6597–6611.
- [81] E. Urban, S. Jacob, M. Nemethova, G. P. Resch, J. V. Small, Electron tomography reveals unbranched networks of actin filaments in lamellipodia, *Nature Cell Biology* 12 (5) (2010) 429–435.
- [82] O. Medalia, I. Weber, A. S. Frangakis, D. Nicastro, G. Gerisch, W. Baumeister, Macromolecular architecture in eukaryotic cells visualized by cryoelectron tomography, *Science* 298 (5596) (2002) 1209–1213.
- [83] C. A. Larabell, M. A. Le Gros, X-ray tomography generates 3-D reconstructions of the yeast, *saccharomyces cerevisiae*, at 60-nm resolution, *Molecular Biology of the Cell* 15 (3) (2004) 957–962.
- [84] H. Wolter, Spiegelsysteme streifenden Einfalls als abbildende Optiken für Röntgenstrahlen, *Annalen der Physik* 10 (1952) 94–114, 286.
- [85] R. H. Mole, The LD₅₀ for uniform low LET irradiation of man, *British Journal of Radiology* 57 (677) (1984) 355–369.
- [86] R. L. Chaput, R. T. Kovacic, Miniature pig performance after fractionated supralethal doses of ionizing radiation, *Radiation Research* 44 (3) (1970) 807–820.
- [87] A. P. Casarett, C. L. Comar, Incapacitation and performance decrement in rats following split doses of fission spectrum radiation, *Radiation Research* 53 (3) (1973) 455–461.
- [88] H. Ito, H. Watanabe, M. Takehisa, H. Iizuka, Isolation and identification of radiation-resistant cocci belonging to the genus *deinococcus* from sewage sludges and animal feeds, *Agricultural and Biological Chemistry* 47 (6) (1983) 1239–1247.

- [89] P. M. Bennett, G. F. Foster, C. J. Buckley, R. E. Burge, The effect of soft X-radiation on myofibrils, *Journal of Microscopy* 172 (1993) 109–119.
- [90] J. Kirz, C. Jacobsen, M. Howells, Soft x-ray microscopes and their biological applications, *Quarterly Reviews of Biophysics* 28 (1) (1995) 33–130.
- [91] X. Zhang, C. Jacobsen, S. Lindaas, S. Williams, Exposure strategies for PMMA from *in situ* XANES spectroscopy, *Journal of Vacuum Science and Technology B* 13 (4) (1995) 1477–1483.
- [92] T. Beetz, C. Jacobsen, Soft x-ray radiation-damage studies in PMMA using a cryo-STXM, *Journal of Synchrotron Radiation* 10 (3) (2003) 280–283.
- [93] R. Henderson, Cryo-protection of protein crystals against radiation damage in electron and x-ray diffraction, *Proceedings of the Royal Society B* 241 (1300) (1990) 6–8.
- [94] R. L. Owen, E. Rudiño-Piñera, E. F. Garman, Experimental determination of the radiation dose limit for cryocooled protein crystals, *Proceedings of the National Academy of Sciences* 103 (13) (2006) 4912–4917.
- [95] R. D. Leapman, S. Sun, Cryo-electron energy loss spectroscopy: observations on vitrified hydrated specimens and radiation damage, *Ultramicroscopy* 59 (1995) 71–79.
- [96] H. Ade, X. Zhang, S. Cameron, C. Costello, J. Kirz, S. Williams, Chemical contrast in x-ray microscopy and spatially resolved XANES spectroscopy of organic specimens, *Science* 258 (1992) 972–975.
- [97] S. E. Hieber, C. Bikis, A. Khimchenko, G. Schweighauser, J. Hench, N. Chicherova, G. Schulz, B. Müller, Tomographic brain imaging with nucleolar detail and automatic cell counting, *Scientific Reports* 6 (2016) 32156.
- [98] R. Mizutani, R. Saiga, M. Ohtsuka, H. Miura, M. Hoshino, A. Takeuchi, K. Uesugi, Three-dimensional x-ray visualization of axonal tracts in mouse brain hemisphere, *Scientific Reports* 6 (2016) 35061.
- [99] M. Isaacson, M. Utlaut, A comparison of electron and photon beams for determining micro-chemical environment, *Optik* 50 (3) (1978) 213–234.
- [100] E. G. Rightor, A. P. Hitchcock, H. Ade, R. D. Leapman, S. G. Urquhart, A. P. Smith, G. Mitchell, D. Fischer, H.-J. Shin, T. Warwick, Spectromicroscopy of poly(ethylene terephthalate): Comparison of spectra and radiation damage rates in x-ray absorption and electron energy loss, *Journal of Physical Chemistry B* 101 (11) (1997) 1950–1960.
- [101] J. Kirz, Mapping the distribution of particular atomic species, in: D. Parsons (Ed.), *Ultrasoft X-ray Microscopy: Its Application to Biological and Physical Sciences*, Vol. 342 of *Annals of the New York Academy of Sciences*, New York, 1980, pp. 273–287.
- [102] J. Kirz, Specimen damage considerations in biological microprobe analysis, in: *Scanning Electron Microscopy*, Vol. 2, SEM Inc., Chicago, 1980, pp. 239–249.
- [103] A. G. Michette, G. R. Morrison, C. J. Buckley (Eds.), *X-ray Microscopy III*, Vol. 67 of *Springer Series in Optical Sciences*, Springer-Verlag, Berlin, 1992.